

**NASA
Technical
Memorandum**

NASA TM-86565

THE MULTISPECTRAL ATMOSPHERIC MAPPING
SENSOR (MAMS): Instrument Description,
Calibration, and Data Quality

By Gary J. Jedlovec, W. Paul Menzel,
Robert Atkinson, Gregory S. Wilson,
and John Arvesen

Systems Dynamics Laboratory
Science and Engineering Directorate

August 1986

(NASA-TM-86565) THE MULTISPECTRAL
ATMOSPHERIC MAPPING SENSOR (MAMS):
INSTRUMENT DESCRIPTION, CALIBRATION AND DATA
QUALITY (NASA) 42 p

N87-12828

CSSL 14B

G3/35

Unclas
44643



National Aeronautics and
Space Administration

George C. Marshall Space Flight Center

TABLE OF CONTENTS

	Page
I. INTRODUCTION	1
II. INSTRUMENT DESCRIPTION	1
III. FLIGHT DAYS	7
IV. MULTISPECTRAL DATA	7
A. Data and Resolution	7
B. Calibration	10
C. Noise Analysis	19
D. Intercomparison of Data with Other Instruments	26
V. CONCLUSIONS	32
REFERENCES	36

PRECEDING PAGE BLANK NOT FILMED

LIST OF ILLUSTRATIONS

Figure	Title	Page
1.	MAMS optical diagram.....	3
2.	Spectral response curves	5
3.	Infrared spectrum	6
4.	MAMS flight tracks	9
5.	Scanning resolution diagram	11
6.	MAMS channel 12 image 18 May 1985	14
7.	Standard deviation of calibration counts	15
8.	Plot of calibration counts for Figure 6.....	16
9.	MAMS channel 12 image with corrected calibration.....	17
10.	Plot of corrected calibration counts for Figure 9.....	18
11.	MAMS channel 12 image on 14 January 1986.....	20
12.	Plot of raw calibration counts for Figure 11.....	21
13.	Autocovariance function for 2.5 milliradian aperture.....	23
14.	Plot of MAMS noise correlation for 18 May 1985	24
15.	Plot of MAMS noise correlation for 14 January 1986	25
16.	MAMS channel 11 image for 18 May 1985	29
17.	AVHRR channel 4 image for 18 May 1985.....	30
18.	VAS channel 8 image for 18 May 1985.....	31
19.	MAMS channel 11 image for 14 January 1986	33
20.	AVHRR channel 4 image for 14 January 1986.....	34
21.	Composite MAMS water vapor image on 22 January 1985	35

LIST OF TABLES

Table	Title	Page
1.	Daedalus AADS1268 Channel Characteristics	4
2.	MAMS Channel Characteristics	4
3.	VAS and AVHRR Channel Characteristics	4
4.	MAMS Flight Data	8
5.	MAMS Single Sample Noise Determination	26
6.	Intercomparison of NE Δ T	26
7.	Comparison of Simulated Data for MAMS, VAS, and AVHRR Bands	27
8.	Comparison of Observed Data for MAMS, VAS, and AVHRR Bands	28

TECHNICAL MEMORANDUM

THE MULTISPECTRAL ATMOSPHERIC MAPPING SENSOR (MAMS): INSTRUMENT DESCRIPTION, CALIBRATION, AND DATA QUALITY

I. INTRODUCTION

Multispectral infrared imagery of the Earth's atmosphere and surface for meteorological applications are currently being obtained from polar orbiting platforms by the NOAA and DMSP series meteorological satellites and from geostationary platforms by the GOES and METEOSAT. The geostationary imagery is unique because global and mesoscale thermal, moisture, cloud field, and cloud motion information can be derived every 30 min. Despite its improved spatial and temporal sampling resolution over polar orbiting atmospheric imagers and sounders, a quantitative description of the atmosphere's thermal and moisture structure seems limited to the larger mesoscales of motion (i.e., features with wavelengths greater than 100 to 200 km) [1]. Smith et al. [2], Chesters et al. [3,4], and Petersen et al. [5] have indicated some hope of finer resolution of moisture fields with VAS water vapor imagery. However, quantitative verification of these results is rare because of the scarcity of verifying data and because of the considerable radiometric noise in individual field of view measurements which cause uncertainty in the derived fields.

While moderate mesoscale resolution of atmospheric features is available with infrared measurements from VAS, the broad band visible sensor (0.55 to 0.75 μm) provides finer horizontal resolution of reflected solar radiation from clouds and surface features. Many studies have been performed with this 1 km visible information for detecting clouds and cloud systems, cloud tracking on both the global and mesoscales, severe storm diagnosis and monitoring, and precipitation estimation. However, the incompatibility between the spatial resolution and scanning geometry of the visible and infrared sensors is a serious problem and has restricted the combined use of these measurements in atmospheric studies.

The Multispectral Atmospheric Mapping Sensor (MAMS) has been developed in order to combine high resolution visible and infrared measurements to study small scale atmospheric moisture variability, to monitor and classify clouds, and to investigate the role surface characteristics may play in the production of clouds, precipitation, and severe storms. The visible and infrared bands share the same optical configuration and therefore have the same spatial resolution. Although developed as an aircraft instrument, the design of a future space-borne sensor, in low Earth or geostationary orbit, with similar monitoring capabilities is possible. The intent of the document is to describe the aircraft instrument, data resolution and calibration, and the absolute accuracy of the measurements by intercomparison with other instruments.

II. INSTRUMENT DESCRIPTION

The MAMS is a multispectral scanner which was developed by modifying NASA's airborne Thematic Mapping Sensor (TMS, Daedalus AADS1268). (A complete description of the Daedalus instrument can be found in Daedalus [6]). The dichroic and

bandpass filters in the spectrometer of the TMS were changed to enable spectral sampling in two water vapor absorption channels in addition to the 11 μm window channel in the infrared region.

The MAMS is capable of producing high resolution imagery in the visible and infrared channels with detailed spectral resolution. From a high altitude aircraft at 20 km, the horizontal ground resolution of each individual field of view is 50 m when the 2.5 mrad optics are in place (100 m if the larger 5.0 mrad optics are used). The width of the entire cross path field of view is roughly 40 km, providing detailed resolution over a relatively large area where convective activity may be present.

The MAMS has two major components, the scan head and the spectrometer (Fig. 1). The scan head consists of the primary collecting telescope, a rotating scan mirror, a motor encoder assembly, and two controlled thermal sources. The field of view, defined by the aperture, is available in two different sizes, 2.5 mrad and 5.0 mrad. The larger aperture degrades the horizontal resolution by a factor of two in each direction and changes the visible channel bandwidths, but allows four times as much energy to reach the detectors for better signal-to-noise characteristics. The scan head is housed in an Invar steel and aluminum structure to shield it from the elements and to join it with the spectrometer.

The spectrometer consists of optical elements which spectrally separate the polychromatic input energy, lenses which focus the separated energy onto sensors, detectors which convert optical energy to an electrical signal, and preamplifiers which condition the signal. The energy collected by the spectrometer is separated into four distinct optical paths using dichroic filters; three paths for the infrared data (one for each spectral band) and one for the visible and near infrared data.

The spectrometer detectors are of two types, silicon for the visible radiation and mercury cadmium telluride for the thermal infrared radiation. The visible detector is an eight element array which converts optical energy to electrical energy. The physical edges of the array and the shape of each band's spectral response are determined by the dispersion characteristics of the prism placed in the optical path and the location of the array in the dispersed beam. The individual band edges are determined by the location of the gaps between elements of the array. The spectral characteristics of the TMS (Daedalus [7]) and the MAMS visible channels (Osterwisch [8]) are listed in Tables 1 and 2.

The thermal infrared detectors are each housed in a vacuum dewar which contains a cooled long wave filter and defines both edges of the particular spectral band. These band widths are presented in Table 2. Each infrared detector has an associated preamplifier to process the electrical signal.

The spectral response functions for the three infrared channels of the MAMS are shown in Figure 2; they were specified to be similar to the 6.7, 11.2, and 12.7 μm channels on VAS, and somewhat less similar to the 10.8 and 11.8 μm channels on the higher resolution AVHRR imagery (NOAA series polar orbiters). Table 3 presents these channel characteristics for comparison to those of MAMS in Table 2.

Figure 3 presents a portion of the infrared absorption and emission energy spectrum for the Earth/atmospheric system along with the MAMS channel locations. In the center of the diagram (8.0 to 13 μm) lies the atmospheric window where roughly half of the thermal energy emitted by the Earth escapes to space. MAMS channels 11 (VAS 8, AVHRR 4) and 12 (VAS 7, AVHRR 5) sense energy in this

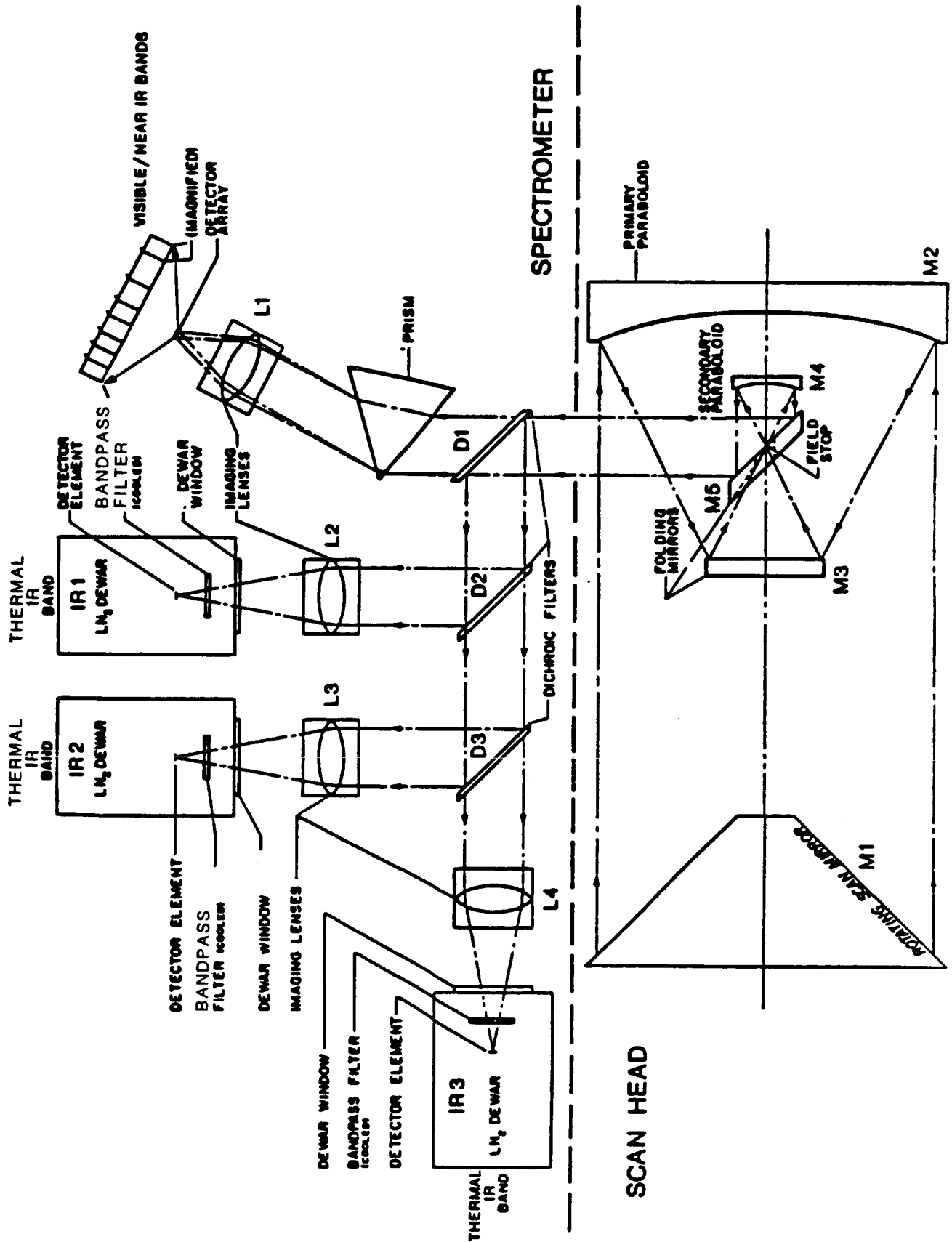


Figure 1. MAMS spectrometer and scan head optical diagram.

TABLE 1. DAEDALUS AADS1268 CHANNEL CHARACTERISTICS

Channel	Spectral Range (μm)	
	2.5 mrad	
1	0.42 - 0.45	
2	0.45 - 0.52	
3	0.52 - 0.60	
4	0.60 - 0.62	
5	0.63 - 0.69	
6	0.69 - 0.75	
7	0.76 - 0.90	
8	0.91 - 1.05	
9	1.55 - 1.75	
10	2.08 - 2.35	
11 & 12 ^a	8.50 - 13.0	

- a. These channels have the same spectral characteristics although the scene data in each channel is digitized using different gains and offsets, yielding different dynamic ranges of the values.

TABLE 2. MAMS CHANNEL CHARACTERISTICS

Channel	Spectral Range (μm)	
	2.5 mrad	5.0 mrad
1	0.42 - 0.45	0.42 - 0.45
2	0.45 - 0.52	0.45 - 0.52
3	0.52 - 0.60	0.52 - 0.60
4	0.60 - 0.62	0.57 - 0.67
5	0.63 - 0.69	0.60 - 0.73
6	0.69 - 0.75	0.65 - 0.83
7	0.76 - 0.90	0.72 - 0.99
8	0.91 - 1.05	0.83 - 1.05
9	6.20 - 6.90	6.20 - 6.90
10 & 11 ^a	10.32 - 12.02	10.32 - 12.02
12	12.20 - 12.56	12.20 - 12.56

- a. On flights before January 1986, channel 10 was used as a redundant 6 micron channel. Channel 9 sensed the cold range while 10 sensed the warm range. Currently, channels 10 and 11 are used similarly for the 11 micron data.

TABLE 3. INFRARED CHANNEL CHARACTERISTICS FROM VAS AND AVHRR

Channel		Spectral Range (μm)	
VAS	AVHRR	VAS	AVHRR
10	-	6.40 - 7.00	-
8	4	10.38 - 12.12	10.35 - 11.25
7	5	12.53 - 12.82	11.43 - 12.37

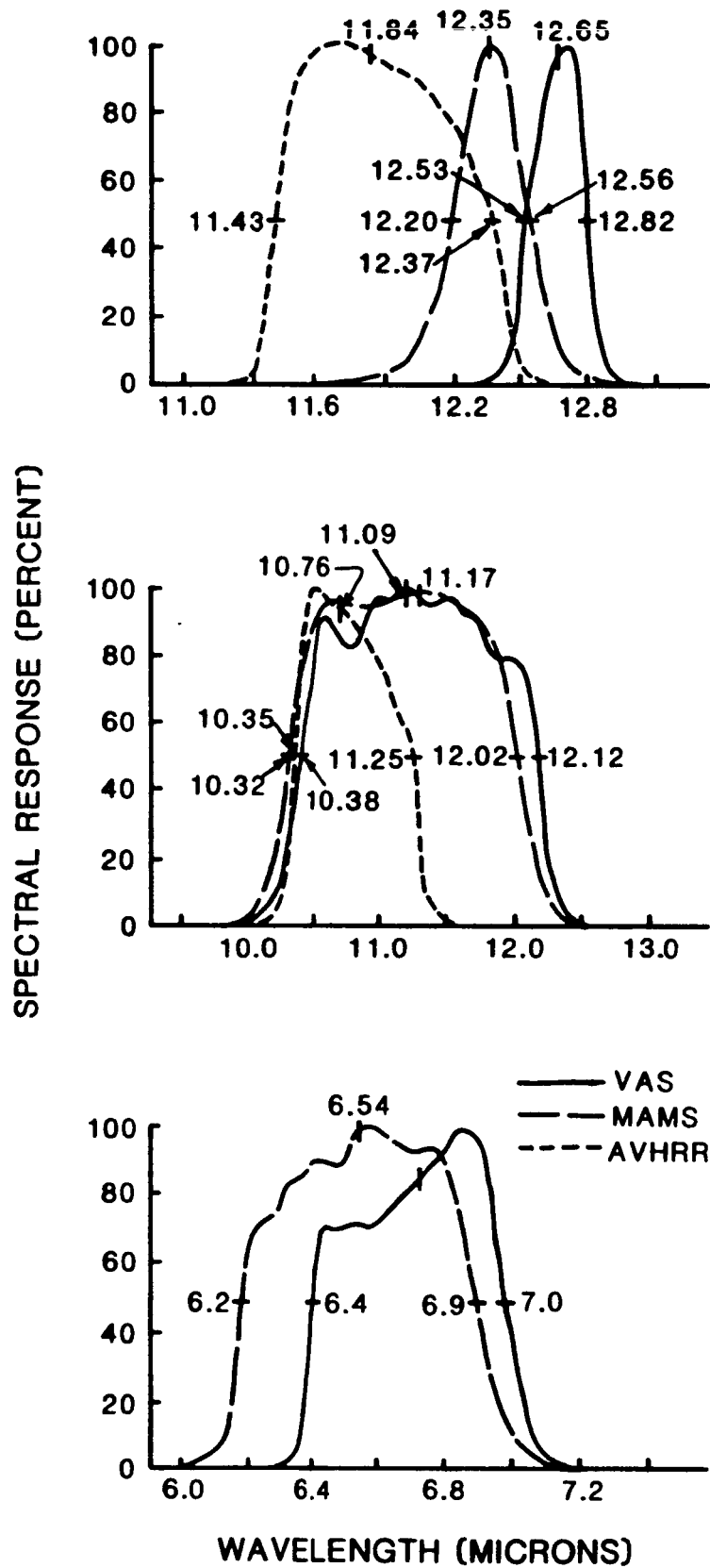


Figure 2. Response curves indicating the sensitivity of the MAMS, VAS, and AVHRR instruments in the (a) 11 μm, (b) 12 μm, and (c) 6 μm regions.

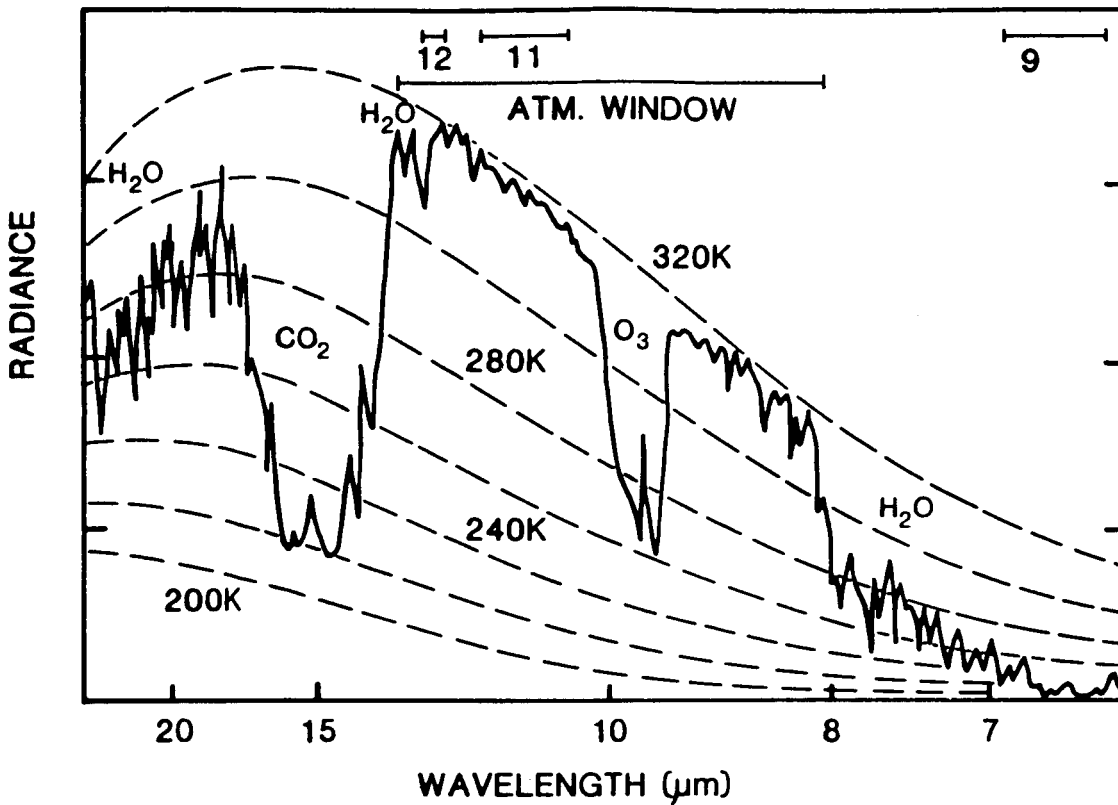


Figure 3. Typical infrared emission and absorption spectrum showing the position of the MAMS bands in relation to the transparent and absorbing portions of this region.

window region, however, channel 12 with its narrow bandwidth selectively measures radiation from the Earth which is partially affected by water vapor absorption.

MAMS channel 9 is in the water vapor absorption band (Fig. 3) and is comparable to VAS 10. Radiation sensed in this region of the infrared spectrum comes from the re-emission of energy absorbed by water vapor in the middle and upper portion of the troposphere. The layer from which this measured radiation originates varies with temperature and moisture content and typically ranges from 700 to 300 mb.

The visible and near infrared portion of the sensor offer high spectral resolution (Tables 1 and 2). Traditionally, these channels have been useful because of the selective scattering characteristics of land, water, and vegetation. The meteorological applications of the visible and near infrared channels can be directed at both the land-water surfaces and cloud features using the same selective scattering principles. It should be noted that when the 5.0 mrad optics are used (to achieve better signal to noise ratios in the IR channels), the spectral bands in the visible region become broader than those of the TMS. The affect of this on the usefulness of the visible data has yet to be determined.

III. FLIGHT DAYS

The MAMS has been flown on a NASA U-2/ER-2 high altitude aircraft for both engineering checkout flights and scientific missions. Flight dates and general information are listed in Table 4. While the January 1985 flights served primarily as engineering checkout of instrument and/or hardware problems, many interesting atmospheric and land features were observed with the instrument. In particular, mountain wave features in the lee of the Sierra Nevadas were observed in the water vapor imagery from 22 January.

The MAMS flights during May and June 1985 were conducted to sample a variety of weather conditions and also corresponded to a period of special ground-based observations of the Pre-STORM field experiment (Purdum et al. [9]). General flight tracks from which MAMS data were collected are shown in Figure 4. Additionally, these flights coincided with simultaneous observations made from the AVHRR and VAS. Section IV.D of this report presents an intercomparison of these measurements in order to evaluate the absolute accuracy of the MAMS calibration procedures.

Several days are of particular interest. The first part of the 18 May flight contained ocean data, which provided an ideal situation to study the noise characteristics of the MAMS over a relatively stable background scene. Corresponding data from the VAS and AVHRR were available over this region at approximately the same time. Also, 20 and 24 May and 26 June are interesting because they sampled a humid summertime environment preceding thunderstorm activity. Flights on the 22 and 23 June were constructed such that four passes over the same area region occurred at one hour intervals, thereby providing high horizontal resolution with increased temporal frequency to monitor environmental changes.

The MAMS flights in January 1986 tested several new configurations for improving the signal-to-noise ratios. The speed of the scan head was halved (as well as the digitizing rate) and the 5.0 mrad aperture was thoroughly tested. From the data of these four flights, it was apparent that the signal-to-noise was substantially improved.

IV. MULTISPECTRAL DATA

A. Data and Resolution

The instantaneous field of view (ifov) of an instrument is the basic information element in a line scanning system. For the MAMS, the ifov values of 2.5 or 5.0 mrad are possible by interchanging the lens apertures. If the ifov of the instrument is denoted by α , then the ground spot size of the instrument ifov, GR, depends only on the distance $H \sec^2 \theta$ and is expressed as

$$GR_c = \alpha H \sec^2 \theta \text{ (cross track, x direction)} \quad (1a)$$

$$GR_a = \alpha H \sec \theta \text{ (along track, y direction)} \quad (1b)$$

TABLE 4. 1985/86 MAMS FLIGHT INFORMATION

Date	Location	Track	Aperture	Comments
1985				
1-21	CA	E/W over Bay area	2.5	Instrument problems; data unusable
1-22	CA	N/S Central Valley	2.5	Noise in channel 12; lee waves in channel 9
1-24	CA	N/S over Bay area	5.0	Severe droop; data of little use
5-6	CA	San Luis Res	2.5	Good align; some microphonics
5-8	West	Ferry to Topeka	2.5	Data good; channel 12 noise 0.9
5-9	KS/OK	Flight Track A	2.5	Data good
5-12	KS/OK	Flight Track B	2.5	Data good
5-16	KS/OK	Flight Track A	2.5	Data good
5-17	West	Ferry back to Ames	2.5	Data good; pick up HIS
5-18	CA/AZ	Enroute to Yuma	2.5	Ocean data good; hot ground over Yuma
5-19	KS/OK	Flight Track A	2.5	Clear; ahead of squall line
5-20	KS/OK	E/W over border	2.5	Thunderstorms in area
5-21	KS/OK	Displaced Track A	2.5	No HIS; MAMS channel 12 filter fell off
5-23	KS/OK	Displaced Track A	2.5	Saturation in channel 11 (hot ground)
5-24	West	Return to Ames	2.5	Channel 11 offset changed by 20
6-22	KS/OK	Flight Track C	2.5	Time continuity flight
6-23	KS/OK	Flight Track C	2.5	Time continuity flight
6-24	KS/OK	Flight Track C	2.5	Pre-t-storm env.; Fujita flight
6-26	KS/OK	"L" TOP-DUR-AMA	2.5	In front of squall line
8-21	CO	N/S over Denver	2.5	HIS; sat in channel 11; no channel 12
1986				
1-9	CA	Santa Catalina Is.	2.5	12.5 rps
1-10	CA	Santa Catalina Is.	2.5	6.25 rps
1-14	CA	Pacific Ocean	5.0	6.25 rps
1-16	CA	Santa Catalina Is.	5.0	6.25 rps

where H is the height above the ground and θ is the angle from nadir (Fig. 5). For the large aperture and a height of 19.8 km, the scene size is 99.0 x 99.0 m directly below the instrument (nadir). This ground spot size increases by a factor of $\sec^2\theta$ with respect to the x coordinate and $\sec\theta$ with respect to the y coordinate as points away from nadir are scanned. At the edge of the MAMS field of view (43 deg), this ground spot size becomes 185.1 x 135.4 m for the 5.0 mrad aperture. Similar calculations have been made with the smaller 2.5 mrad optics.

To determine the amount of oversampling, the instrument scan speed and aircraft velocity must also be taken into account. The position of the aircraft (and therefore the center of the nadir ifov) from one scan to the next can be computed as

$$P = \frac{V}{S} \quad (2)$$

where V is the true aircraft ground velocity and S is the scan speed. True ground velocity is the sum of the aircraft velocity and the wind velocity. Using the appropriate values for the MAMS flights ($V = 740$ km/hr, $S = 6.25$ rev/sec), $P = 32.9$ m. Therefore, for every scan, the position of the ground ifov moves 32.9 m. Since the ifov is 99.0 m, there is a 67 percent $[(99.0 - 32.9)/99.0]$ overlap of every scan line with the previous one. Thus, when every third scan line is considered, less than a 1 percent overlap occurs. The overlap can be used to good advantage by averaging three consecutive scan lines together to reduce the noise in the scene. For targets above the Earth surface (e.g., clouds), this overlap decreases since the spot size decreases as a function of target distance below the aircraft.

B. Calibration

Data taken from the MAMS is digitized at 716 points across the scanline for each channel and recorded on high density magnetic tape. In addition to the scene data, every scanline includes calibration data which is collected at the beginning and end of the scan by viewing a warm and a cold blackbody source. The following paragraphs describe how this data is used in the calibration of the infrared channels.

For a given spectral band, the radiance $R(T)$ is determined from temperature T through the convolution of the spectral response function $F(\nu)$ and the Planck function $B(T, \nu)$, where ν represents the wavenumber. This is written

$$R(T) = \int_0^{\infty} B(T, \nu) F(\nu) d\nu / \int_0^{\infty} F(\nu) d\nu \quad (3)$$

The spectral response functions were shown in Figure 2. For easier radiance determinations equation (3) is approximated by

$$R(T) = B(T, \nu_c) \quad (4)$$

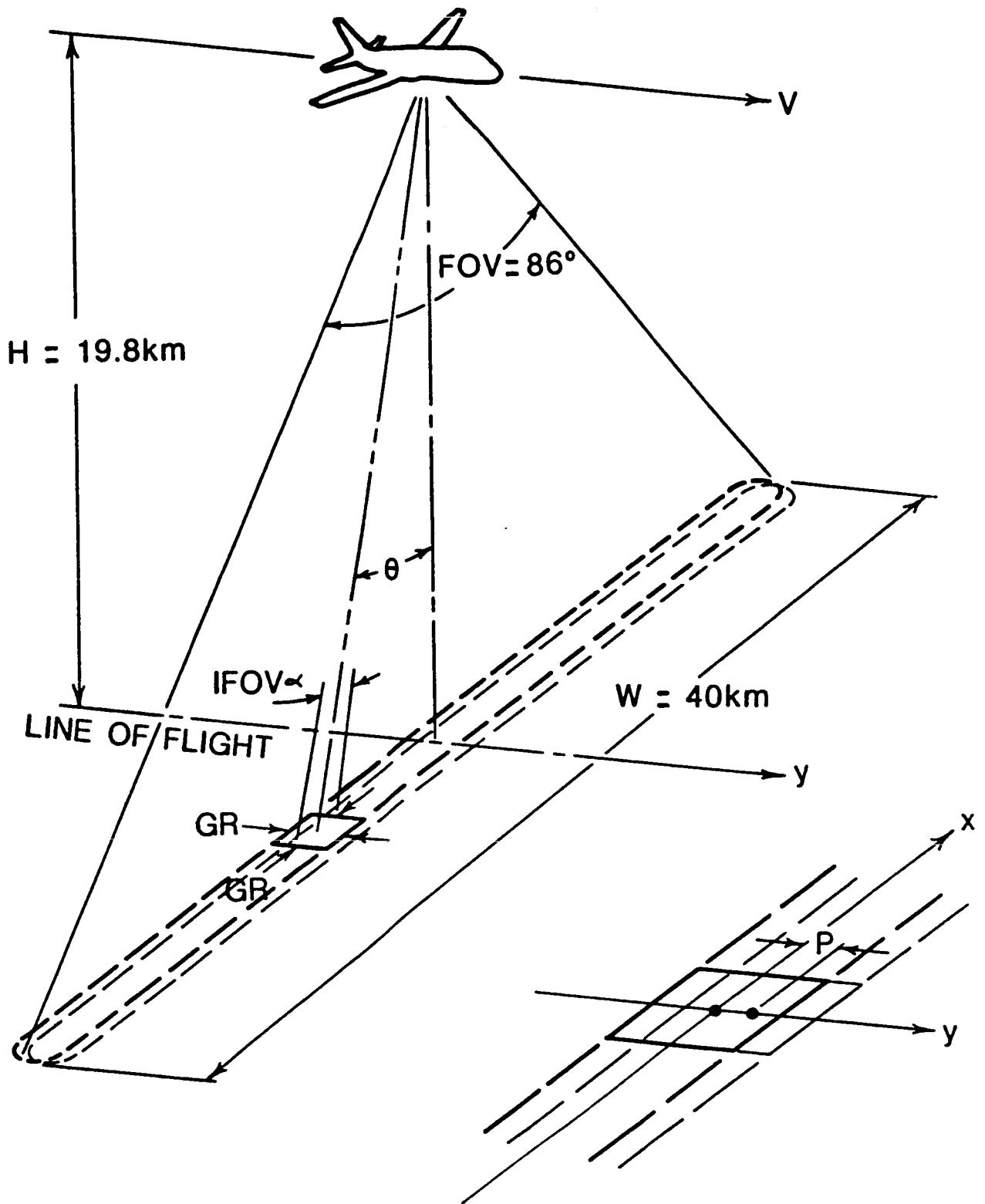


Figure 5. Scanning geometry for the MAMS instrument in the Q-Bay of a NASA U2/ER2 aircraft. Insert shows position of the center of the nadir ifov for two adjacent scans.

where ν_c is the wavenumber that best tracks the variations with temperature. The three MAMS infrared spectral bands have ν_c values of 1528, 902, and 810 cm^{-1} for channels 9, 11, and 12, respectively.

The amount of energy being received by the detector is related to the digitized scene count values through the linear form

$$R_i = a_i + b_i C_i \quad (5)$$

where R_i is the radiance measured in each infrared channel i , C_i is the raw count value in the scene, a_i is the gain or the slope, and b_i is the offset or intercept.

Prior to flight, the gain and offset for each channel are electronically adjusted to minimize the likelihood of saturation over hot scenes and to maximize the effective operating range for each channel. Channel 9 operates from 210 to 280°K and channels 11 and 12 operate from 230 to 330°K; therefore, channel 9 has a gain of roughly 0.3°K/1 count and channels 11 and 12 have a gain of roughly 0.5°C/1 count. The radiance versus count relationship is calculated using the two blackbody sources of known temperatures. Laboratory tests have shown this relationship to be linear over the expected range of scene temperatures (a fractional nonlinearity of less than 5×10^{-4} was observed for the three spectral bands). Thus, we write

$$b_i = \frac{R_{hi} - R_{ci}}{C_{hi} - C_{ci}} \quad (6)$$

$$a_i = \frac{C_{ci}R_{hi} - C_{hi}R_{ci}}{C_{ci} - C_{hi}}$$

where the h and c subscripts denote the hot and cold blackbodies, respectively.

Count values for the blackbodies are an average of several samples.

These coefficients are determined for every scanline and used in equation (5) to calibrate the scene counts along that line. The calibrated values (radiances) then can be transformed into temperatures using the inverse of the Planck function

$$T = \frac{f_2 \nu_i}{\ln \left[\frac{f_1 \nu_i^3}{R} + 1 \right]} \quad (7)$$

where f_1 and f_2 are known constants.

These temperatures can be converted to eight bit count values for storage or display using a number of conversion schemes. A two-piece linear scheme utilized for GOES VISSR/IR imagery has been employed thus far (Bauer and Lienesch [10]). Truncation errors of less than 0.5°C are experienced.

Figure 6 represents a MAMS channel 12 image calibrated using the above procedure. The image has been enhanced to visually bring out details in the scene. The most notable feature is the warm island in the middle of a relatively cool ocean scene. Also obvious is the horizontal variation or stripping from line to line and over groups of lines.

Typically, the counts corresponding to the blackbodies are averaged over several samples, producing a more reliable calibration value. Recent adjustments in the electronic circuitry have changed the number of samples from one to eight. The count values from surrounding lines are also averaged together to reduce the random noise in the count values. Tests have shown that blackbody counts from roughly ten lines yield the most effective calibration of the data (Fig. 7), so that radiometric integrity and image quality are preserved. Striping in the MAMS images is due not only to random line to line noise in the blackbodies as discussed above, but also to a longer period correlated noise in the blackbody counts (Fig. 8). The counts themselves may fluctuate together since DC restore values are used to determine a line offset before each scan. These values are computed from average radiance of the blackbodies from the previous line. This will not affect the calibration when both of the count values (C_h and C_c) float together. However, when the counts do not fluctuate together, an error is introduced into the calibration procedure that can be as large as 2 to 3°K. The cause of this correlated noise is unclear, but it seems related to the signal-to-noise ratio since it is least prevalent in channel 11 and affects the warm blackbody source more than the cold one. Vibrations in the instrument itself may induce correlated noise of this type and affect the scene data as well as the calibration counts. Eliminating the correlated noise without changing the real DC restore fluctuations should eliminate the striping and reduce the correlated noise in the scene data during the calibration process.

In order to reduce the striping in the MAMS calibrated images, a multiple line average of the counts corresponding to the blackbodies is performed to reduce the random noise in the data and the hot blackbody counts are ignored. Since the fluctuations in the cold count values appear more reliable (presumably because the effects of noise are more apparent at warmer temperatures), the averaged cold count values are used to re-create the warm count values in the following way

$$C_w' = \frac{R2 - R1}{\frac{\Delta R}{\Delta C}} + \overline{C_c} \quad (8)$$

where the response slope $\Delta R/\Delta C$ is a constant based on several hundred lines. The calibration procedure then proceeds as described above by developing a slope and intercept based on the averaged $\overline{C_c}$ and new C_w' values and corresponding temperatures.

This modification provides a relative calibration of the infrared data, but an absolute calibration may depend on empirical adjustments after intercomparisons with VAS and AVHRR. Figure 9 presents the calibrated image based on this procedure and Figure 10 presents the new calibration counts for each scan line. It is apparent

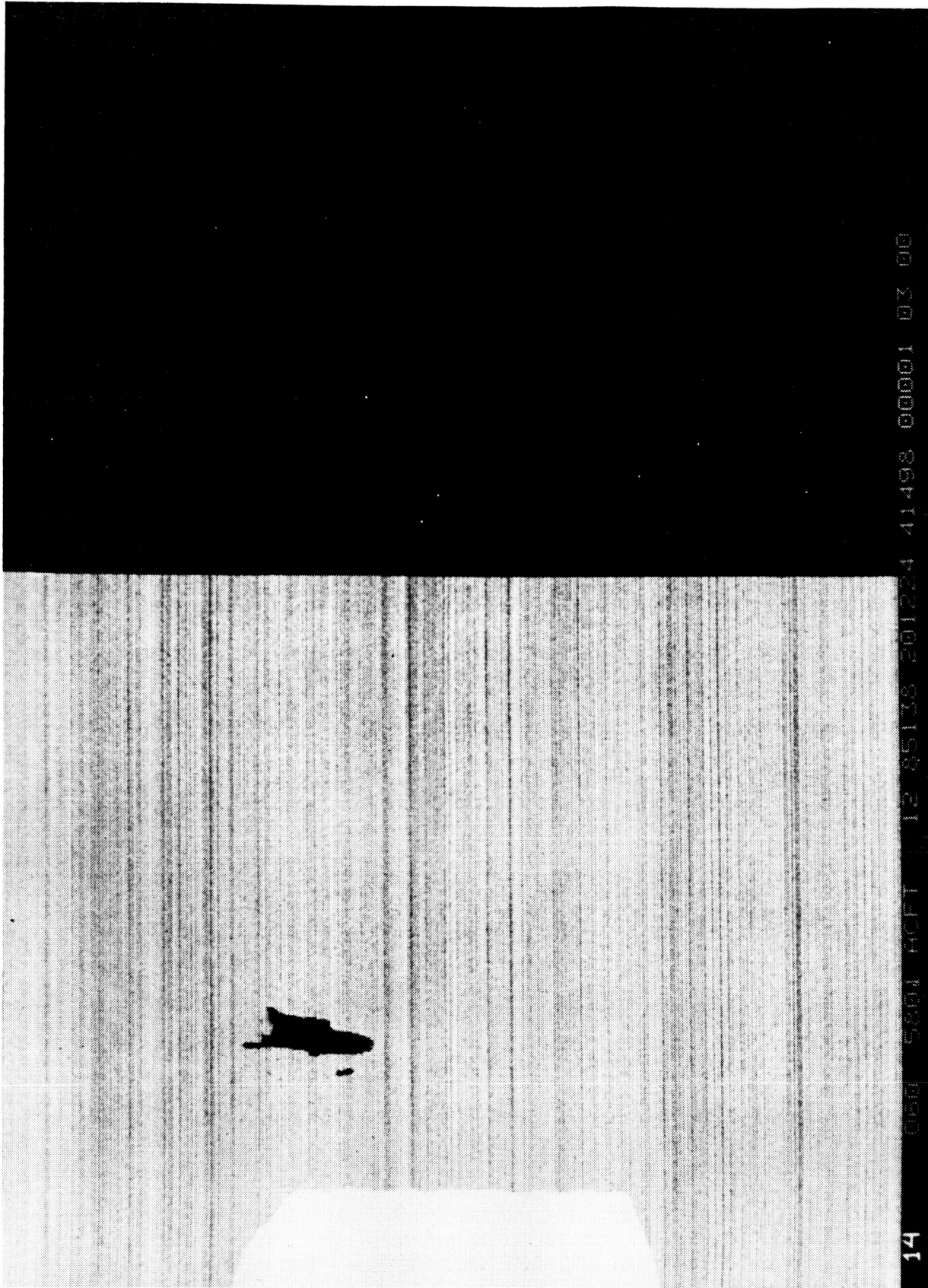


Figure 6. MAMS channel 12 (12.3 μm) image over Santa Barbara Island, CA, on 18 May 1985 at 2012 GMT. The image was produced using the raw calibration counts for each scan line.

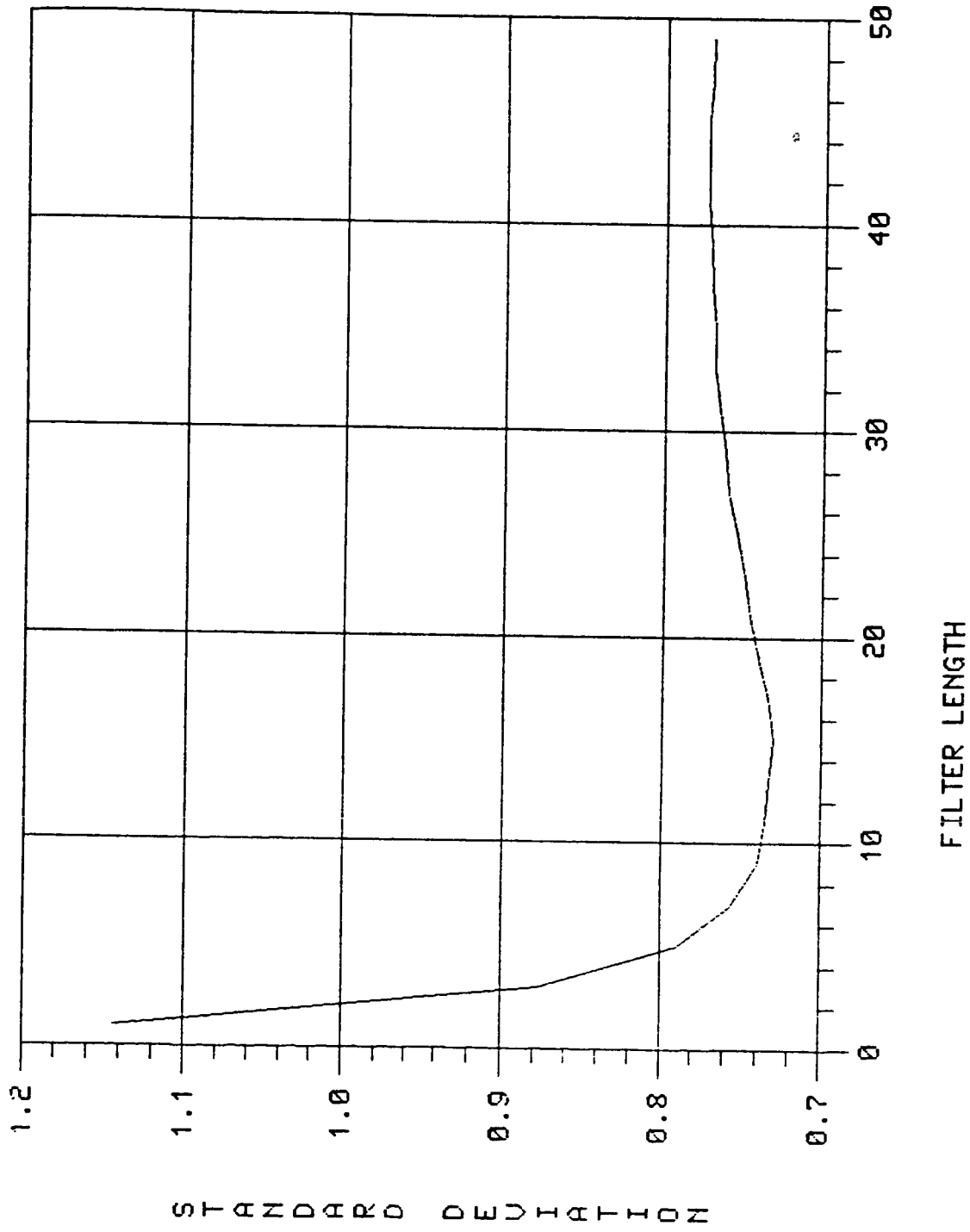


Figure 7. Standard deviation of the average temperature per scan line (\bar{T}_s) as a function of filter length. The filter is a simple arithmetic average of surrounding scan lines.

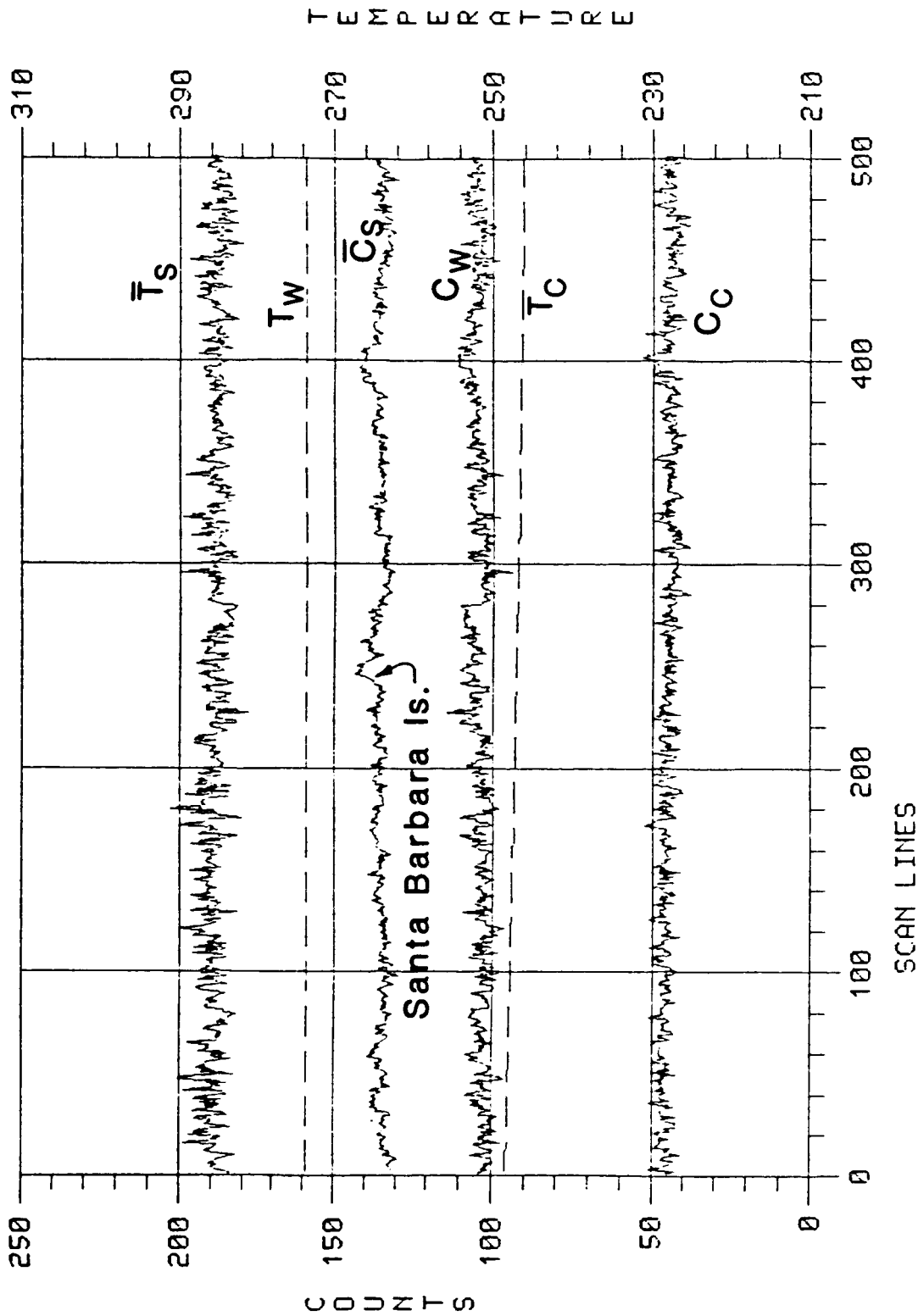


Figure 8. Plot of raw calibration counts and black body temperatures as a function of scan line for the image in Figure 6. The subscripts c and w denote cold and warm calibration sources, respectively. C_s is the average of the raw counts along each scan line and T_s the average of the calibrated counts converted to temperature. Note that Santa Barbara Island is present in the raw counts, but not in the line average calibrated values.

A proper calibration should not remove this feature.

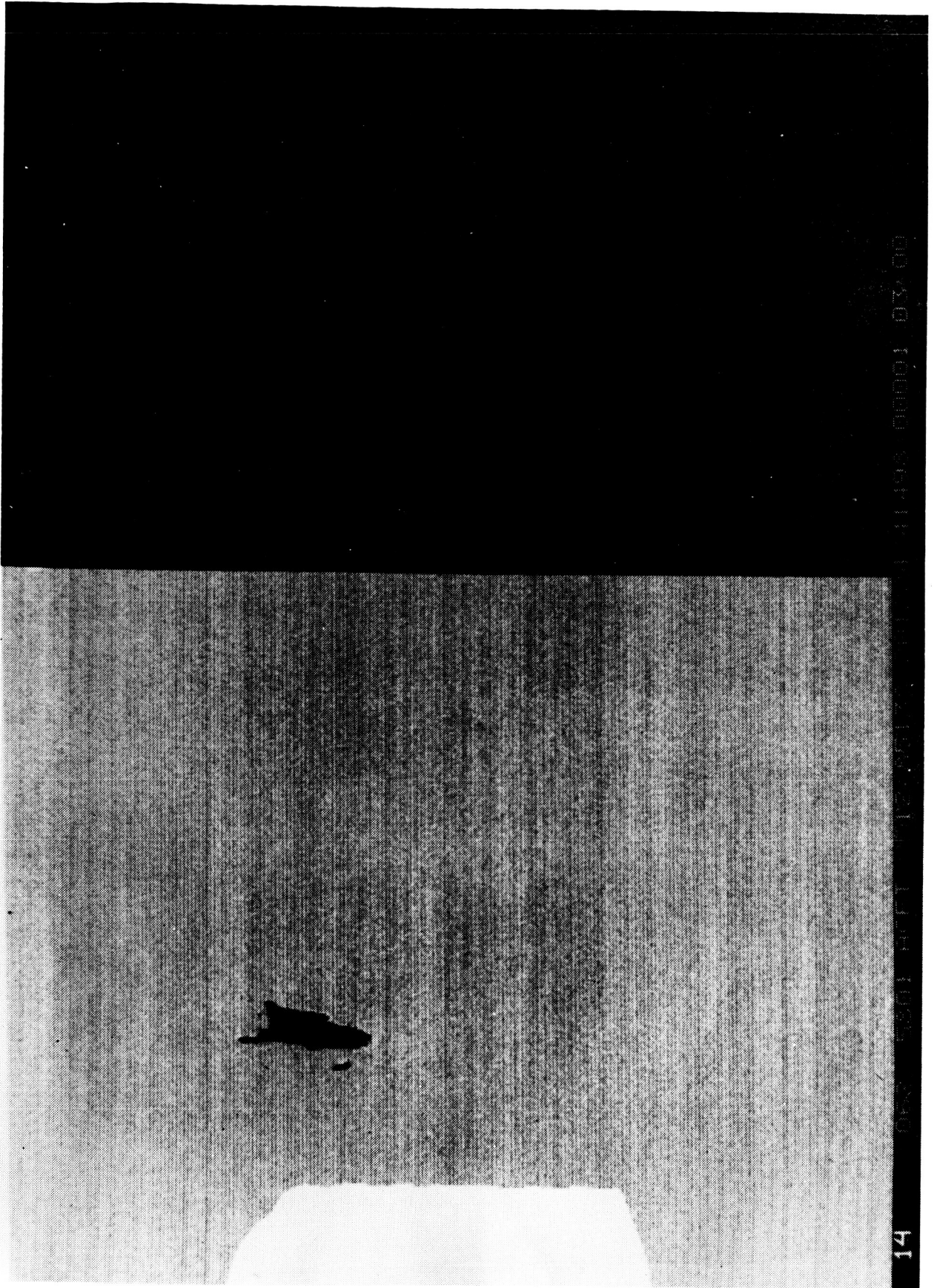


Figure 9. Same as Figure 6, except that the corrected calibration procedure is used.
Note the reduction in line-to-line variation.

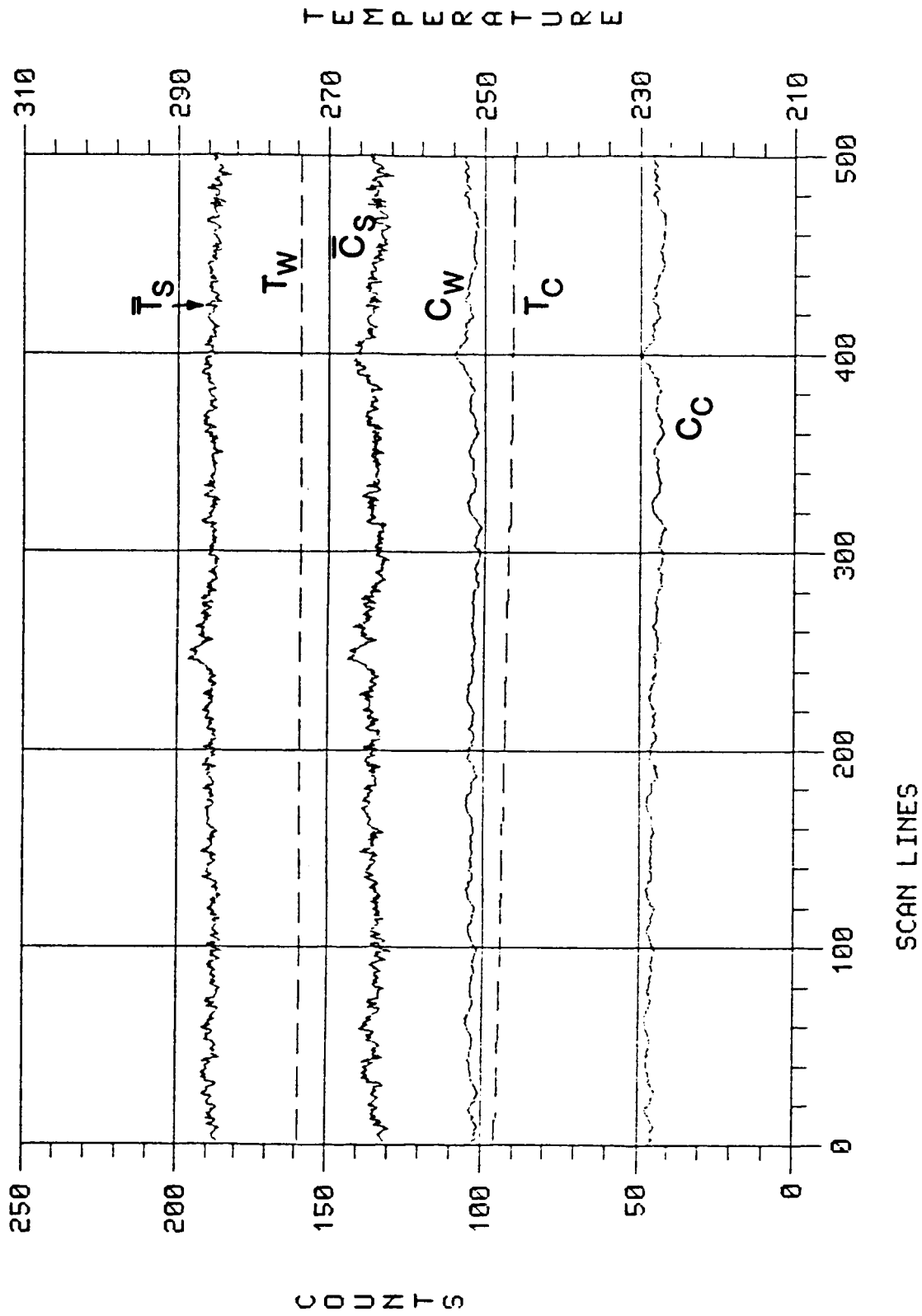


Figure 10. Same as Figure 8, except for the correct calibration counts and scene calibrated values. The line-to-line variability in the scene temperature T_s is reduced and the island is also present in the plotted data.

from a comparison of this scene with the one in Figure 6 that the striping has been reduced. However, not all of the striping can be eliminated without substantially changing the absolute calibration of the entire image. An examination of the average scene values for each line both before (raw data) and after calibration show this feature. However, a recent reconfiguration of the MAMS has reduced these effects considerably.

More recent MAMS data does not exhibit these coherent noise and calibration problems. The 6.25 rps/5.0 mrad aperture configuration of the 14 and 16 January 1986 flights reduces these problems considerably so that the single line calibration described by equations (5) and (6) can be employed. An example of this data with the simple calibration procedures is presented in Figure 11. Figure 12 displays the raw calibration count values corresponding to a section of this image. By comparing this to Figure 8, a dramatic improvement is seen. An equally dramatic improvement in the calibrated image is also apparent (compare to Figs. 6 and 9). This is the MAMS configuration preferred for future flights.

C. Noise Analysis

The infrared detectors on MAMS exhibit some low frequency noise so that samples taken at roughly 26 microsecond intervals (the nominal sampling rate for a spin rate of 12.5 revolutions per second) will experience noise contributions with significant correlation. This implies that the standard error of the average of N MAMS infrared measurements will be larger than σ/\sqrt{N} . To determine how much larger, the expected variance of the means of samples of size N is written

$$\sigma_M^2 = E[(M - \mu)^2] = E(M^2) - \mu^2 \quad (9)$$

where μ is the population mean (assumed to be zero for simplicity), and M is the mean of N detector noise voltage samples, $e(t_i)$, which is given by

$$M = \frac{1}{N} \sum_{i=1}^N e(t_i) \quad , \quad (10)$$

and E denotes the expectation value

$$E[e(t)e(t+\tau)] = \lim_{T \rightarrow \infty} \frac{1}{T} \int_{-T/2}^{+T/2} e(t)e(t+\tau) dt \quad (11)$$

which is just the autocovariance function $C(\tau)$. Then

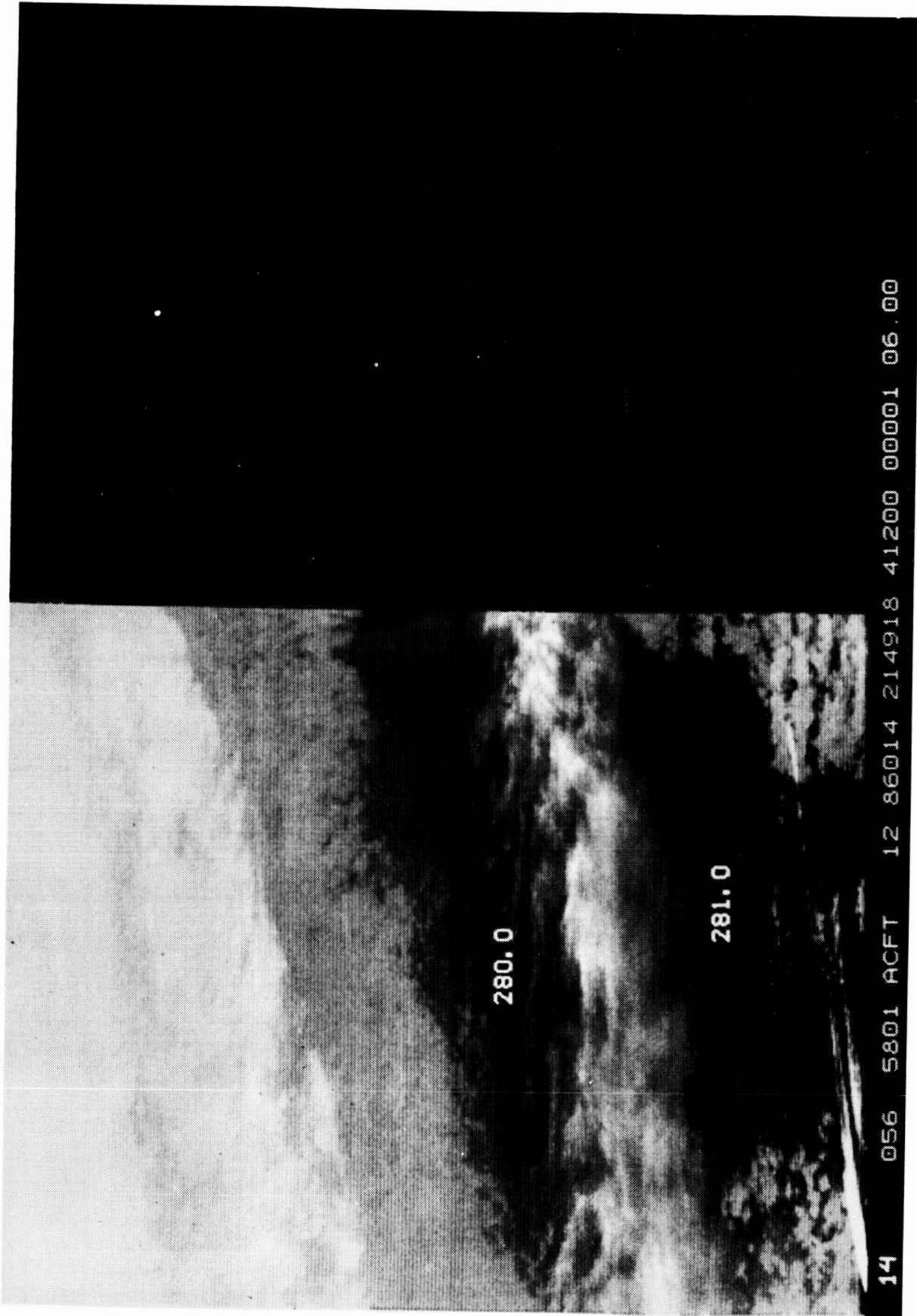


Figure 11. Single line calibration of MAMS channel 12 (12.3 μm) image over Monterey, CA, on 14 January 1986 at 2149 GMT. Multiple level clouds are present in the upper half of the image as bright (cold) features and high cirrus clouds with low emissivity over the water region. The darker regions represent the warmer surface temperatures over the land.

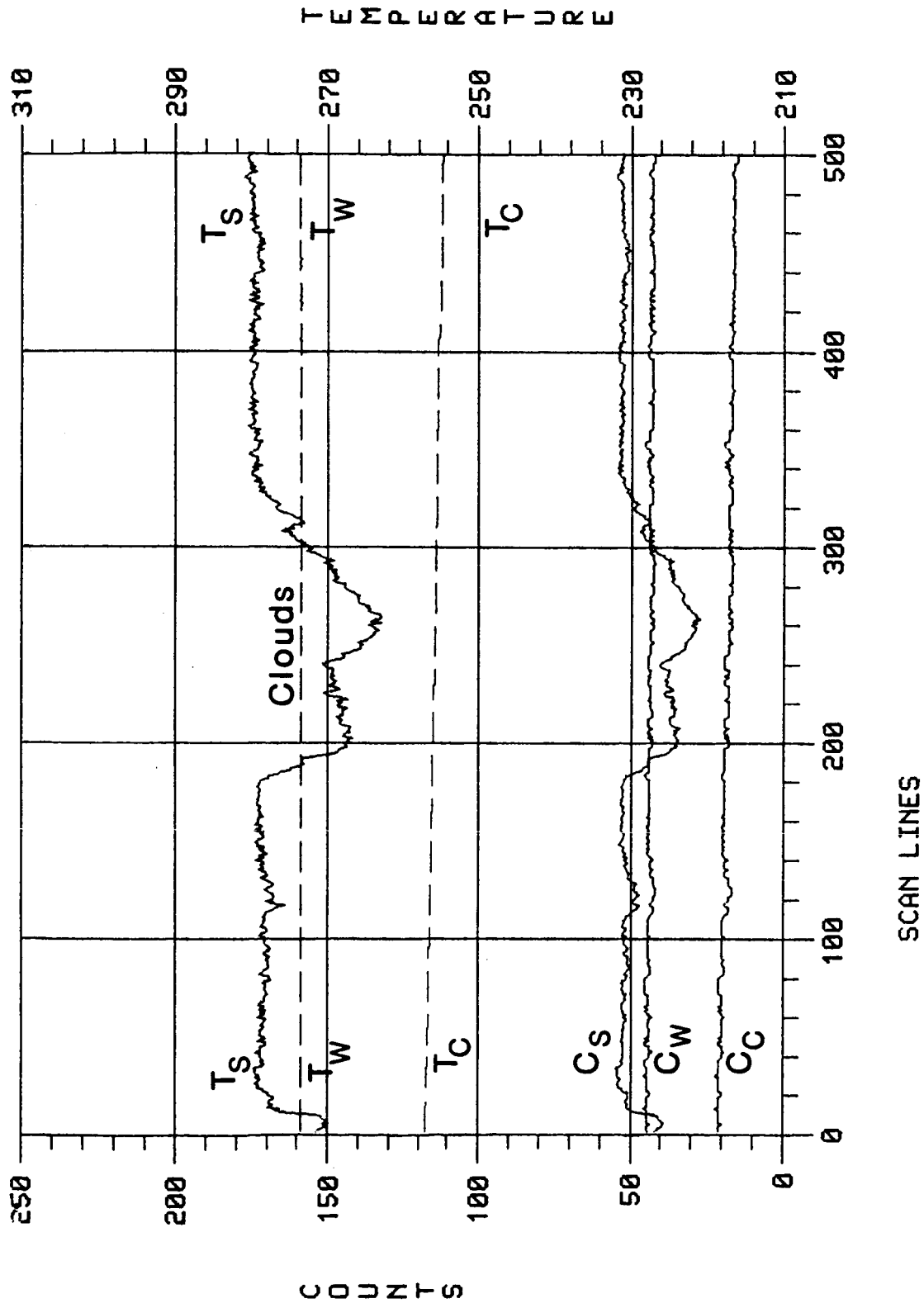


Figure 12. Plot of the raw calibration counts and black body temperatures for a portion of the image in Figure 11. The smoothness of these curves reflect the improved noise characteristics in the latest instrument configuration.

$$\sigma_M^2 = \frac{1}{N^2} \sum_{i=1}^N \sum_{j=1}^N E[e(t_i)e(t_j)] = \frac{1}{N^2} \sum_{i=1}^N \sum_{j=1}^N C(t_j - t_i) \quad (12)$$

But the signal variance is defined as

$$\sigma^2 = \lim_{T \rightarrow \infty} \frac{1}{T} \int_{-T/2}^{+T/2} [e(t)]^2 dt = C(0) \quad (13)$$

so

$$\sigma_M^2 = \frac{\sigma^2}{N} + \frac{1}{N^2} \sum_{i=1}^N \sum_{j \neq i}^N C(t_j - t_i) \quad (14)$$

This shows explicitly the effect of noise correlation. If $e(t_i)$ and $e(t_j)$ were random independent variables, then we would have $C(t_j - t_i) = 0$ for $i \neq j$ and $\sigma_M^2 = \sigma^2/N$. Since $e(t_i)$ and $e(t_j)$ are correlated, a considerably different result is obtained.

Evaluation of the autocovariance function from raw data produced during the engineering checkout flights of May 1985 (2.5 mrad aperture, 12.5 rev/sec) allows calculation of σ_M^2/σ^2 as a function of sample number. Figures 13 and 14 show the plots of $C(\tau)$ and σ_M^2/σ^2 for the three HgCdTe detectors (11.1 micron data of channel 11, 6.5 micron data of channel 9, and the 12.3 micron data of channel 12). The covariance of the noise is comparable in channels 9 and 11, and diminished in channel 12. The degree of smoothness in these curves indicates the noise level of the channel signal. The noise reduction after averaging ten consecutive samples, measured by σ_M^2/σ^2 , is 0.21, 0.20, and 0.13, respectively, for channels 9, 11, and 12. The uncorrelated value of $1/N$ is 0.10. Therefore, the noise, after averaging along a scan line for channels 9 and 11, is roughly two times greater than if the noise were uncorrelated. For channel 12 the noise reduction is more efficient, closer to the $1/N$ value. Figure 15 shows the σ_M^2/σ^2 plot from the January 1986 flight data (5.0 mrad aperture, 6.25 rev/sec). All channels have higher noise correlation from sample to sample, but this is alleviated by the fact that single sample noise values are greatly reduced.

Table 5 summarizes the single sample noise determination from 18 May 1985 flight data (2.5 mrad aperture, 12.5 rev/sec) over the ocean off the California coast (Fig. 6). After calculations involving about 100 samples over a uniform temperature portion of the ocean, the single sample noise values are found to be 0.5, 0.2, and 0.9°C, respectively, for channels 9, 11, and 12. Table 5 also shows the single sample noise

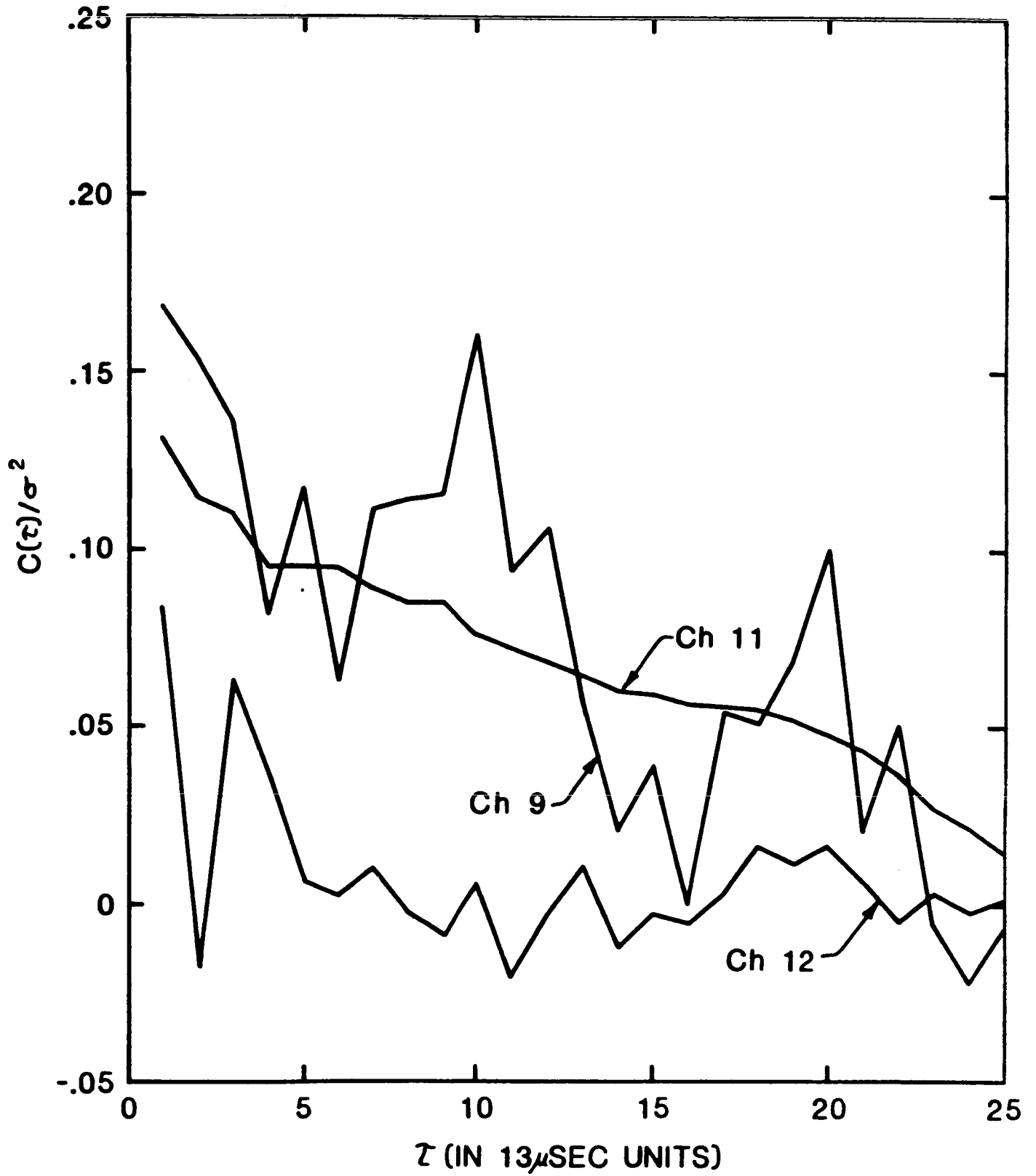


Figure 13. The autocovariance of the three MAMS infrared channels. Sample taken from area in Figure 6.

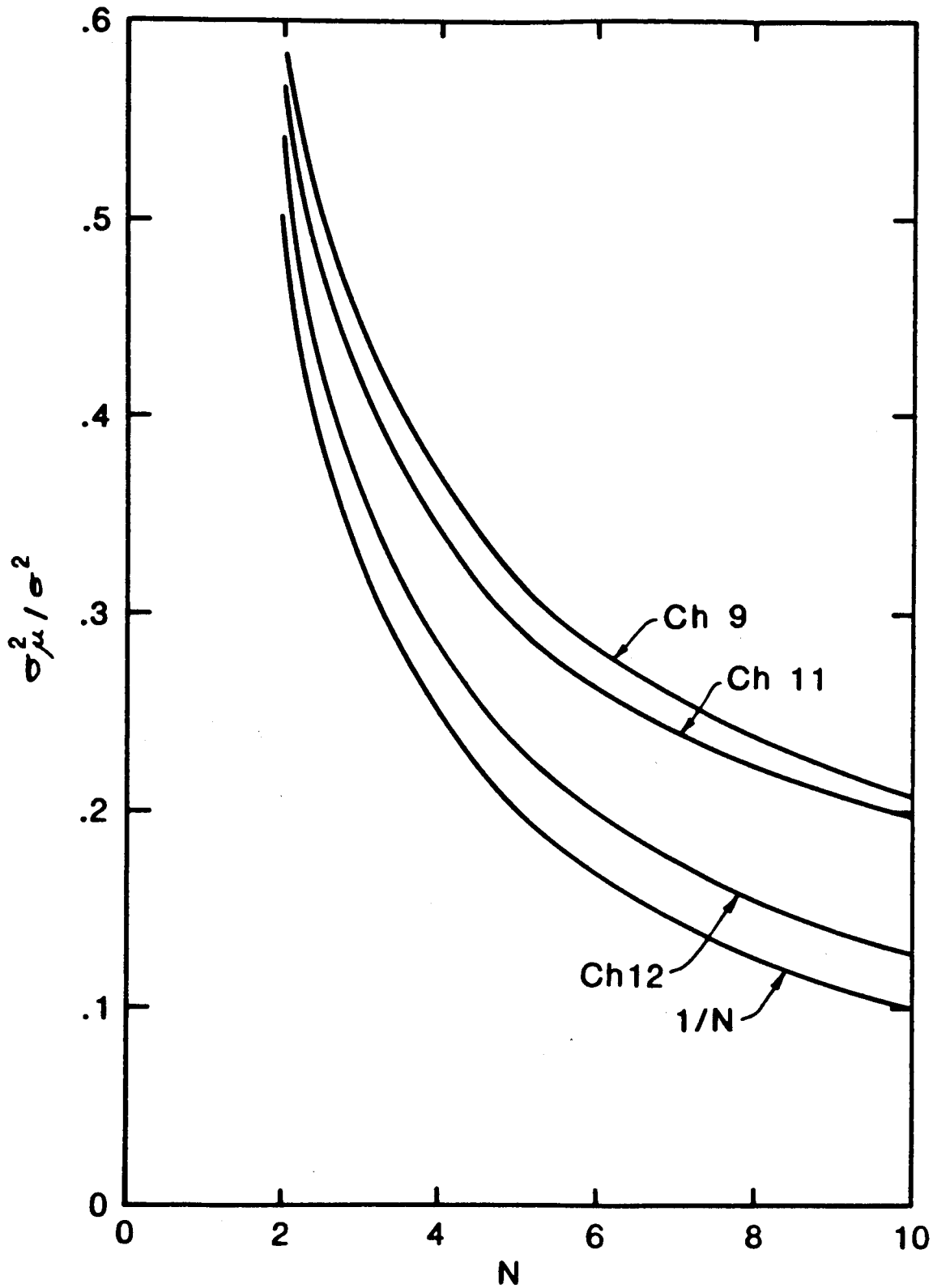


Figure 14. The correlation of noise associated with adjacent pixels of each MAMS infrared channel. Data taken from area shown in Figure 6.

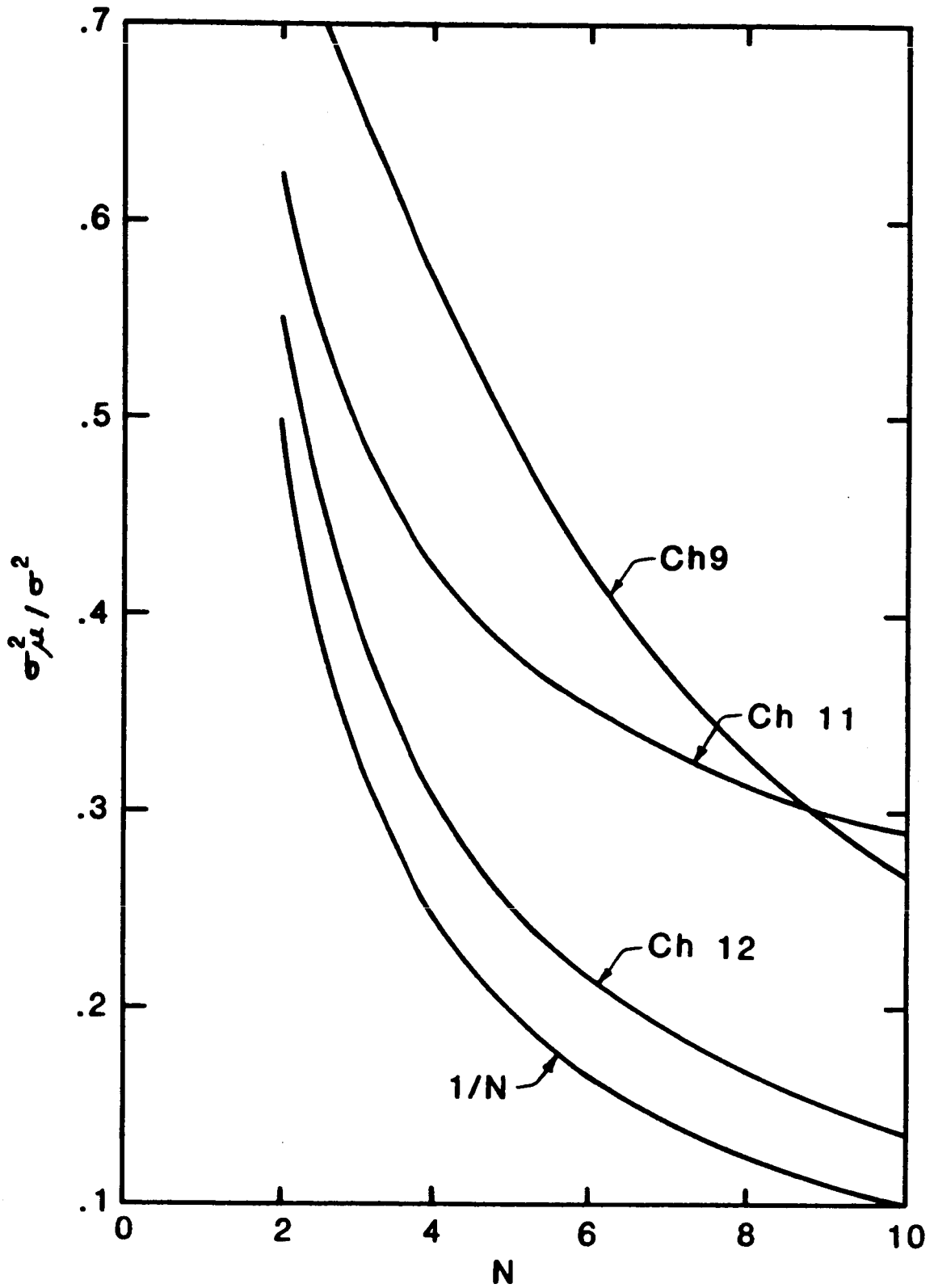


Figure 15. Same as Figure 14, except for the 6.25 rps/5.0 mrad configuration in Figure 11.

values from a comparable flight on 14 January 1986 (5.0 mrad aperture, 6.25 rev/sec) to be 0.3, 0.1, 0.4°K, respectively, for channels 9, 11, and 12. The noise is halved in the latter configuration.

TABLE 5. MAMS SINGLE SAMPLE NOISE

Channel	ν (cm^{-1})	λ (μm)	σ_R ($\text{mw/ster/m}^2/\text{cm}^{-1}$)	2.5 mrad/5.0 mrad Apertures	
				T_{scene} (°K)	σ_T (°K)
9	1528	6.5	0.1/0.1	247/251	0.5/0.3
11	902	11.1	0.3/0.1	288/284	0.2/0.1
12	810	12.3	1.4/0.7	285/279	0.9/0.4

Table 6 shows a comparison of the noise equivalent delta temperatures ($\text{NE}\Delta\text{T}$) available with the three observing systems (MAMS, VAS, and AVHRR). The 12 micron spectral band of the AVHRR has a much smaller $\text{NE}\Delta\text{T}$ than that of MAMS or VAS because its bandpass is much broader. Otherwise, the $\text{NE}\Delta\text{T}$ s are very comparable. The MAMS has not sacrificed signal-to-noise in order to achieve high horizontal resolution.

TABLE 6. INTERCOMPARISON OF $\text{NE}\Delta\text{T}$

	$\text{NE}\Delta\text{T}$ (°K)		
	Band		
	6 micron	11 micron	12 micron
MAMS (2.5/5.0 mrad)	0.5/0.3	0.2/0.1	0.9/0.4
VAS	0.7	0.1	1.0
AVHRR		0.1	0.2

D. Intercomparison of Data with Other Instruments

In order to compare MAMS data with those from similar instruments, it is necessary to first look at simulated data in the respective bands. Figure 2 presents the spectral response curves for the MAMS, VAS, and AVHRR channels of interest. Considering the 11 micron bands, there is much similarity in the MAMS and VAS curves (as designed), but the AVHRR curve covers a slightly different wavelength range. The results of this are presented in Table 7 which shows simulated radiances and brightness temperatures in each band. These radiance values (I) were obtained for each band and sensor from a radiative transfer calculation:

TABLE 7. INTERCOMPARISON OF SIMULATED DATA

Radiances (mW/ster/m ² /cm ⁻¹) Band			
	6 micron	11 micron	12 micron
MAMS	7.86	96.47	109.45
VAS	8.73	97.53	111.57
AVHRR	--	91.895	105.77
Brightness Temperature (°K) Band			
	6 micron	11 micron	12 micron
MAMS	254.83	287.30	285.96
VAS	253.86	287.29	285.38
AVHRR	--	287.31	287.16

$$I_{ij} = R_{ij}[T(\text{sfc})] \tau_{ij}(\text{sfc}) - \int_{P_s}^0 R_{ij}[T(p)] \tau_{ij}(p) dp \quad (15)$$

where τ represents transmittance, R is the radiance defined in equation (3), i corresponds to each instrument (MAMS, VAS, and AVHRR), and j to the particular band (6, 11, and 12 micron). Transmittances were computed using a model (McMillin and Fleming [1]; Fleming and McMillin [12]; and Weinreb and Neuendorffer [13]) with the temperature and moisture data of the Los Angeles sounding at 00 GMT on 19 May 1985. Brightness temperatures are computed from the inverse Planck function [eq. (7)] corrected for monochromaticity. For the 11 micron band, equation (15) produces varying radiances, but nearly identical brightness temperatures. This is expected despite the difference in response functions, since the atmosphere is relatively (or equally) transparent in this region. Differences are more apparent for the 12 micron band where absorption due to atmospheric water vapor is an effect. Since the spectral response functions are positioned differently in this region (Fig. 2), simulated brightness temperatures for each instrument are different. The coldest temperature occurs in the 12 micron band for VAS, with the MAMS being about 0.5°K warmer. The AVHRR temperature is the warmest as expected from the position of the response function with respect to the 12.7 micron absorption region. Even more important is the difference between the 11 and 12 micron bands (referred to as the "split window") for each sensor because of its usefulness for low level moisture and skin temperature determinations. These split window differences are 1.91, 1.34, and 0.15°K for VAS, MAMS, and AVHRR, respectively, and they are expected to vary with atmospheric moisture content. For the 6 micron channel, the spectral response function differences between MAMS and VAS produce simulated brightness temperature differences of about 1.0°K. This is consistent with the shift of the MAMS response function away from the 6.7 micron absorption region.

Imagery from these three instruments were collected simultaneously (within one hour of each other) off the California coast on 18 May 1985 (three hours prior to the simulated data). Table 8 presents a comparison of this data over a region just north of Santa Barbara Island. MAMS was in the 2.5 mrad/12.5 rps configuration, which is its noisiest configuration. Unlike the simulated data for the 11 micron band, the observed data shows some differences between each instrument. The MAMS data in this band is about 1.5°K warmer than that of VAS which is 1.0°K warmer than the AVHRR data. This variability may be explained in part by the uncertainty in the registration of the data from each sensor, particularly the high resolution MAMS imagery where exact registration information is unavailable. Also, the spatial resolution from each sensor is much different (VAS at 7 km, AVHRR at 1 km, and MAMS at 0.05 km at nadir) which compounds the misregistration. Finally, non-nadir viewing of sensors has not been taken into account. A somewhat more appropriate comparison is the split window channel differences between VAS and MAMS, each being about 2.0 to 2.5°K. While this is about 1.0°K greater than the simulated data, time/space discrepancies and the assumed error in the MAMS data may account for this. All things considered, this comparison is quite favorable. The MAMS and VAS 6 micron band differences are also very comparable with VAS being about 1.0°K colder in both cases. The more favorable comparison may be the result of the relatively small spatial variability of mid-tropospheric water vapor detected in these bands (not shown).

TABLE 8. INTERCOMPARISON OF OBSERVED DATA

Radiances (mW/ster/m ² /cm ⁻¹) Band			
	6 micron	11 micron	12 micron
MAMS	6.01	99.94	111.14
VAS	6.80	97.00	111.10
AVHRR	--	99.10	--
Brightness Temperature (°K) Band			
	6 micron	11 micron	12 micron
MAMS	247.15	289.50	287.01
VAS	246.50	287.10	284.81
AVHRR	--	286.03	--

Perhaps a better evaluation of the radiometric performance of the MAMS is seen in Figures 16, 17, and 18 which presents 11 micron imagery from each instrument on 18 May 1985. The relative accuracy of MAMS compares favorably as seen by the grey shade variations across the flight track in each image. This transforms into a 2.0°K brightness temperature gradient for the VAS and AVHRR imagery and slightly more (~3.0°K) for MAMS. Also note the increase in detail provided by the higher resolution MAMS data. A quasi-horizontal ripple pattern (microphonics) is also apparent in the MAMS image (Fig. 16) and is occasionally present in the MAMS data where the scene is relatively unstructured.

ORIGINAL PAGE IS
OF POOR QUALITY

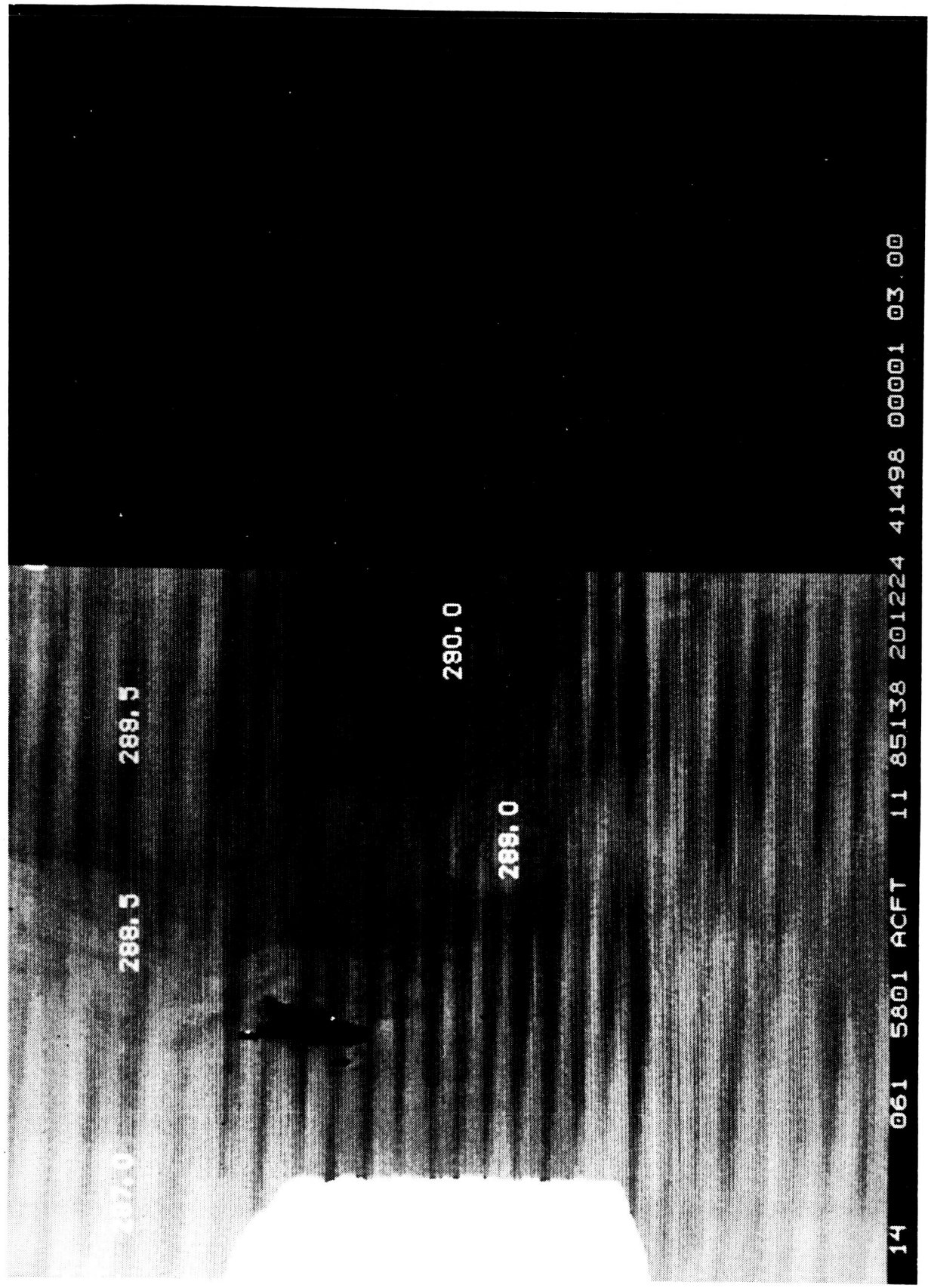


Figure 16. Same as Figure 9, except for MAMS channel 11 (11.2 μm).



Figure 17. AVHRR channel 4 image (10.8 μm) over the region covered by the MAMS image in Figure 16.

ORIGINAL PAGE IS
OF POOR QUALITY

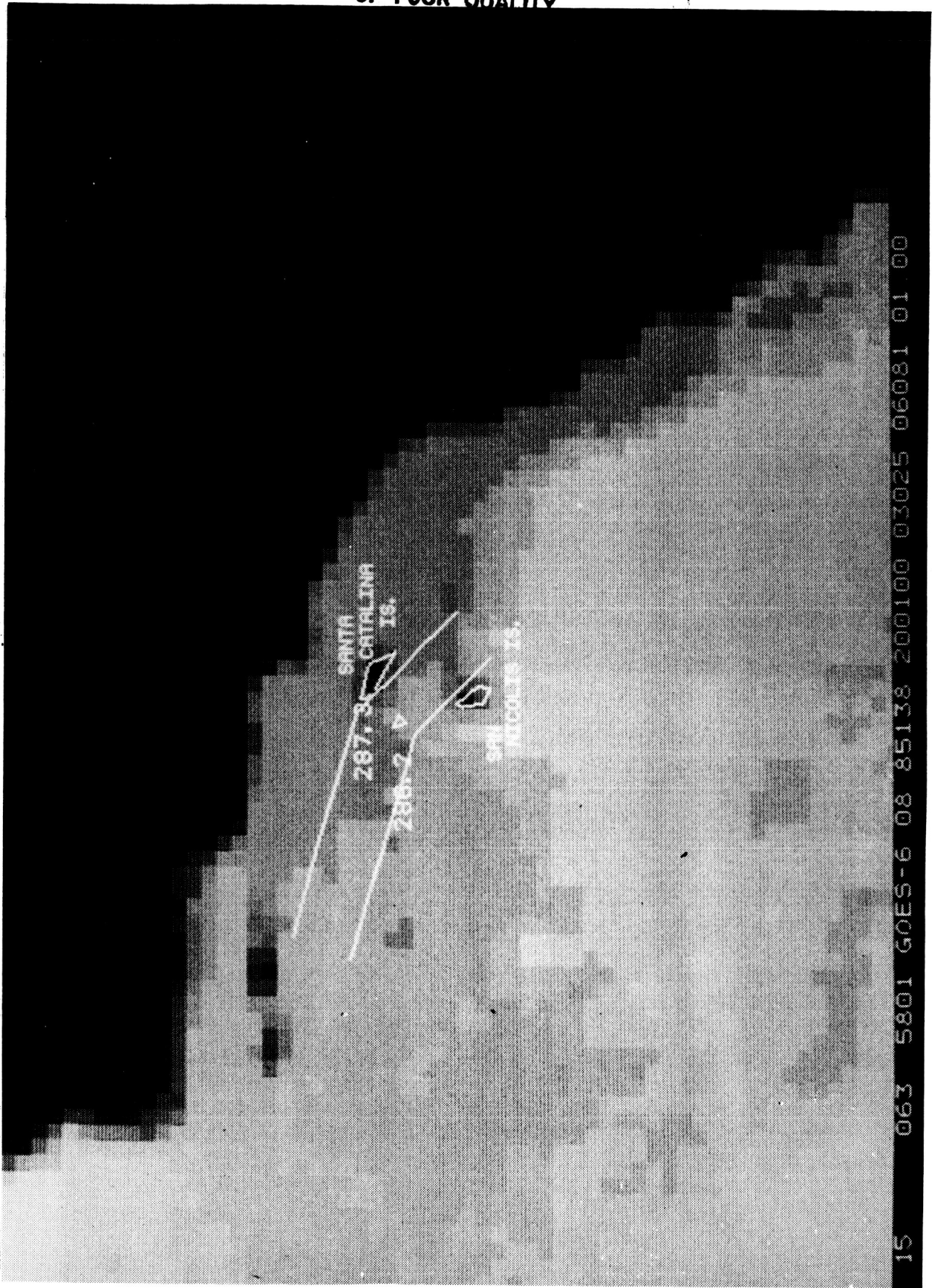


Figure 18. VAS channel 8 image (11.2 μm) over the region covered by the MAMS image in Figure 16.

The configuration changes for the flights on 14 and 16 January 1986 made a substantial improvement to the MAMS imagery as briefly discussed in Section IV.B (Figs. 11 and 12). The 11 micron channel image corresponding to the data previously presented is shown in Figure 19. This data covers an area of clouds and open water off the coast of Monterey, California on 14 January 1986 at 2149 GMT. Figure 20 presents a similar area from the 11 micron channel of AVHRR taken at about the same time. While a 1.0 to 1.5°K temperature difference exists between the indicated spots on the images, this is probably due to the slightly increased water vapor optical depth on the limb of the AVHRR data track. The greatly enhanced MAMS resolution, without loss of radiometric accuracy is apparent in this comparison. VAS data was not available for comparison.

V. CONCLUSIONS

This report presented an overview of a new instrument for providing very high horizontal resolution visible and infrared imagery of atmospheric and surface features. The visible channel imagery was not discussed in detail, since those channels have been documented elsewhere (Daedalus [6]). Considerable effort has gone into analyzing and calibrating the infrared imagery in order to produce accurate quantitative radiance information. For some of the pre-1986 flight data, the absolute calibration needs further investigation, but an accurate portrayal of thermal variations of the Earth's surface and atmospheric water vapor is available. An example is presented in Figure 21. This composite of four adjacent 6.5 μm water vapor images shows signatures of atmospheric wave structures in the lee of the Sierra Nevada mountains of California. These features are not present in the visible imagery (right hand portion of figure). The wavelength of these features is less than 20 km and they would not be well resolved by any other currently available water vapor imagery.

Recent instrument configuration changes to 5.0 mrad aperture and 6.25 rps scan head speed have indicated that single sample noise can be reduced by at least 50 percent if horizontal resolution is degraded to 100 m. This resolution is still an order of magnitude better than resolutions usually available for atmospheric investigations. Single sample noise becomes less than 0.2, 0.1, 0.4°K for the 6, 11, and 12 micron channels, respectively. Better absolute calibration of the radiometric data is also achieved.

Although this report has demonstrated that useful quantitative data is available from the MAMS, some further ideas should be considered.

- o Further improvement in the signal-to-noise ratio of the MAMS channels should not be considered unless improved quantization of the video and blackbody counts is also considered. In the current MAMS configuration, truncation error due to 8-bit representation is larger than the single sample noise in most, if not all, the channels.
- o The channel 12 data would be more advantageous if the bandpass filter were centered at 12.7 μm with a slightly wider bandwidth. This would increase the sensitivity of the channel to low level water vapor.



Figure 19. Same as Figure 11, except for MAMS channel 11 (11.1 μm).

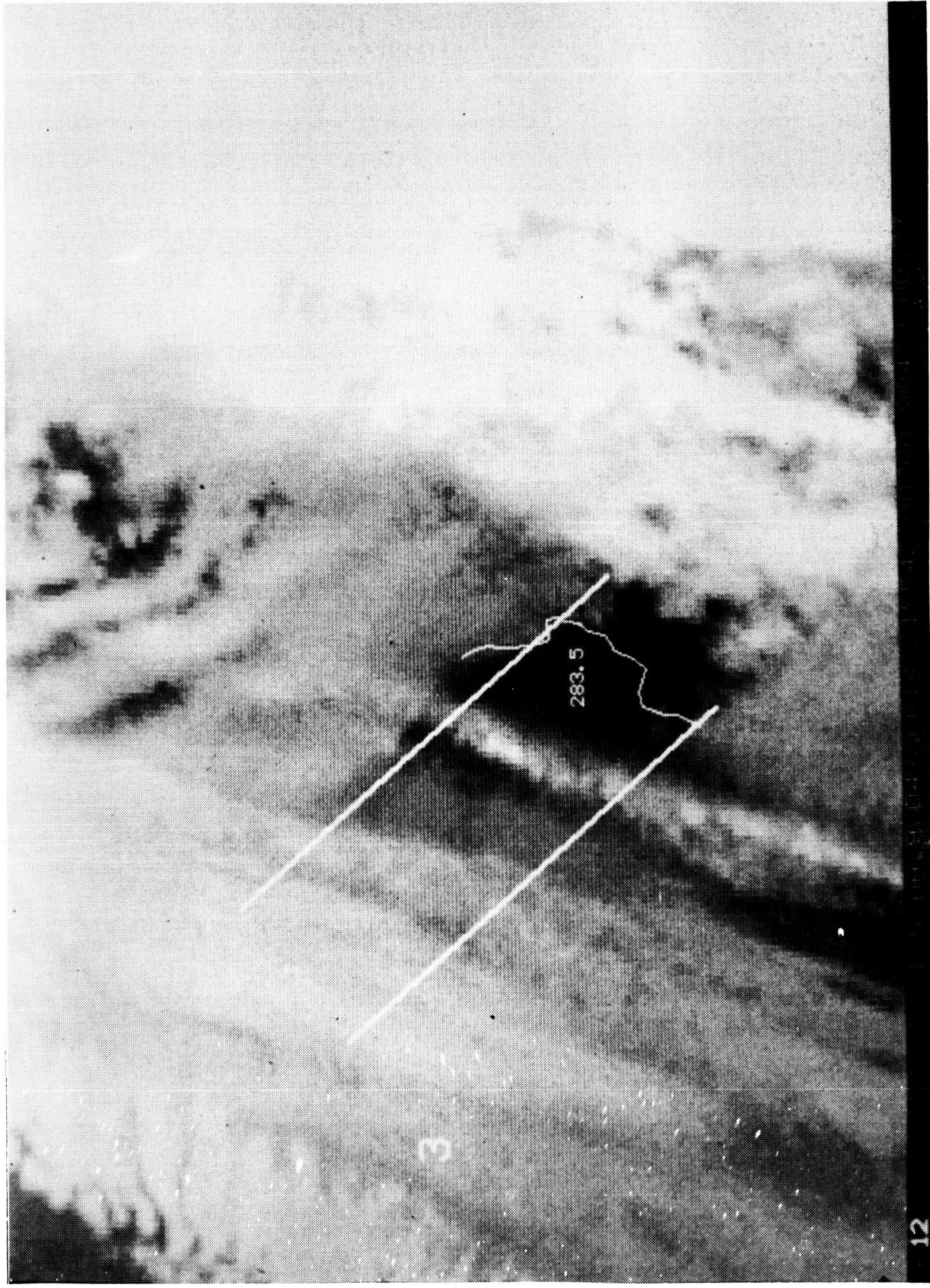


Figure 20. AVHRR channel 4 image (10.8 μm) over the region enclosing the MAMS data of Figure 19.

MULTISPECTRAL ATMOSPHERIC MAPPING SENSOR (MAMS) HIGH RESOLUTION AIRCRAFT COMPOSITE IMAGERY

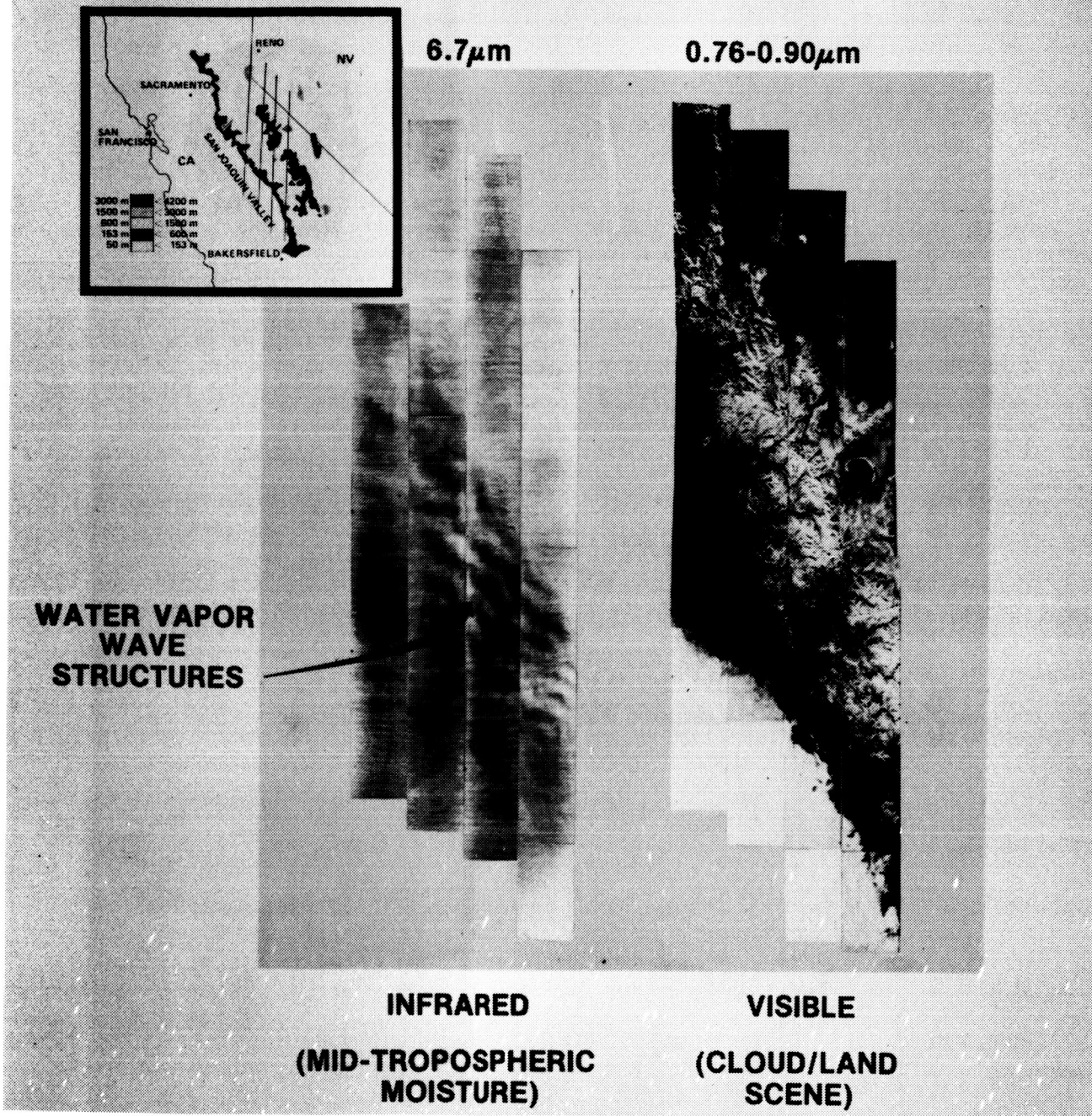


Figure 21. Composite water vapor image from four adjacent MAMS flight tracks on 22 January 1985. The wave-like signatures in the lee of the Sierra Nevada mountains are radiometric responses of varying moisture distributions in a cloud-free environment.

REFERENCES

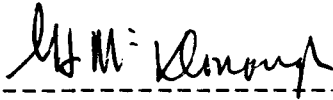
1. Jedlovec, G. J.: An Evaluation and Comparison of Vertical Profile Data from the VISSR Atmospheric Sounder (VAS). *J. Atmos. Ocean. Tec.*, Vol. 2, 1985, pp. 559-581.
2. Smith, W. L., Wade, G. S., and Woolf, H. M.: Combined Atmospheric Sounding/Cloud Imagery - A New Forecast Tool. *Bull. Amer. Meteor. Soc.*, Vol. 66, 1985, pp. 138-141.
3. Chesters, D., Uccellini, L. W., and Robinson, W. D.: Low-Level Water Vapor Fields from the VISSR Atmospheric Sounder (VAS) "Split Window" Channels. *J. Clim. Appl. Meteor.*, Vol. 22, 1983, pp. 725-743.
4. Chesters, D., Uccellini, L. W., and Mostek, A.: VISSR Atmospheric Sounder (VAS) Simulation Experiment for a Severe Storm Environment. *Mon. Wea. Rev.*, Vol. 110, 1982, pp. 198-210.
5. Petersen, R. A., Uccellini, L. W., Mostek, A., and Keyser, D. A.: Delineating Mid- and Low-Level Water Vapor Patterns in a Preconvective Environment Using VAS Moisture Channels. *Mon. Wea. Rev.*, Vol. 112, 1984, pp. 2178-2198.
6. Daedalus: Operator's Manual: AADS1268 Digital Multispectral Scanner System. Daedalus Enterprises, Ann Arbor, Michigan, 1982.
7. Daedalus: Daedalus Scanner Applications...Worldwide: 1982 Comendium. Daedalus Enterprises, Ann Arbor, Michigan, 28 pgs, 1982.
8. Osterwisch, F. G.: MAMS chamber testing and instrument calibration. Daedalus Enterprises, Inc.: System Performance Record. Under NASA contract NAS2-11858, 7 pgs, 1984.
9. Purdom, J. F. W., Green, R. N., Weaver, J. F., Zehr, R. M., and Lubich, D. A.: Satellite Data Support of the Pre-Storm Operations Center. CIRA Paper No. 3, 1985.
10. Bauer, B. and Lienesch, J.: Central Processing and Analysis of Geostationary Satellite Data. NOAA Tech. Memo. NESS 64, C. L. Briston (Editor), 1975, 155 pp.
11. McMillin, L. M. and Fleming, H. E.: Atmospheric Transmittance of an Absorbing Gas: A Computationally fast and accurate transmittance model for absorbing gases with constant mixing ratios in inhomogeneous atmospheres. *Appl. Opt.*, 15, 1976, pp. 358-363.
12. Fleming, H. E. and McMillin, L. M.: Atmospheric Transmittance of an Absorbing Gas. 2: A Computationally Fast and Accurate Transmittance Model for Slant Paths at Different Zenith Angles. *Appl. Opt.*, Vol. 16, 1977, pp. 1366-1370.
13. Weinreb, M. P. and Neuendorffer, A. C.: Method to Apply Homogeneous Path Transmittance Models to Inhomogeneous Atmospheres. *J. Atmos. Sci.*, Vol. 30, 1973, pp. 662-666.

APPROVAL

THE MULTISPECTRAL ATMOSPHERIC MAPPING SENSOR (MAMS):
Instrument Description, Calibration, and Data Quality

By Gary J. Jedlovec, W. Paul Menzel, Robert Atkinson,
Gregory S. Wilson, and John Arvesen

The information in this report has been reviewed for technical content. Review of any information concerning Department of Defense or nuclear energy activities or programs has been made by the MSFC Security Classification Officer. This report, in its entirety, has been determined to be unclassified.



G.F. McDonough
Director
Systems Dynamics Laboratory

1. REPORT NO. NASA TM -86565		2. GOVERNMENT ACCESSION NO.		3. RECIPIENT'S CATALOG NO.	
4. TITLE AND SUBTITLE The Multispectral Atmospheric Mapping Sensor (MAMS): Instrument Description, Calibration, and Data Quality				5. REPORT DATE August 1986	
				6. PERFORMING ORGANIZATION CODE	
7. AUTHOR(S) Gary J. Jedlovec,* W. Paul Menzel,** Robert Atkinson,*** Gregory S. Wilson, and John Arvesen****				8. PERFORMING ORGANIZATION REPORT #	
9. PERFORMING ORGANIZATION NAME AND ADDRESS George C. Marshall Space Flight Center Marshall Space Flight Center, Alabama 35812				10. WORK UNIT NO.	
				11. CONTRACT OR GRANT NO.	
12. SPONSORING AGENCY NAME AND ADDRESS National Aeronautics and Space Administration Washington, D.C. 20546				13. TYPE OF REPORT & PERIOD COVERED Technical Memorandum	
				14. SPONSORING AGENCY CODE	
15. SUPPLEMENTARY NOTES Prepared by Atmospheric Sciences Division, Systems Dynamics Laboratory, Science and Engineering Directorate.					
16. ABSTRACT A new instrument has been developed to produce high resolution imagery in eight visible and three infrared spectral bands from an aircraft platform. An analysis of the data and calibration procedures has shown that useful data can be obtained at up to 50 m resolution with a 2.5 milliradian aperture. Single sample standard errors for the measurements are 0.5, 0.2, and 0.9°K for the 6.5, 11.1, and 12.3 μm spectral bands, respectively. These errors are halved when a 5.0 milliradian aperture is used to obtain 100 m resolution data. Intercomparisons with VAS and AVHRR measurements show good relative calibration. MAMS development is part of a larger program to develop multispectral Earth imaging capabilities from space platforms during the 1990s. *University of Wisconsin-Madison, Space and Engineering Center. **NOAA/NESDIS Advanced Satellite Products Project, Madison, Wisconsin. ***General Electric Co. ****NASA Ames Research Center, Moffett Field, California.					
17. KEY WORDS Multispectral imagery Radiometric calibration Blackbody temperatures Radiances Single sample noise, Coherent noise, Spectral response, Sensitivity			18. DISTRIBUTION STATEMENT Unclassified - Unlimited		
19. SECURITY CLASSIF. (of this report) Unclassified		20. SECURITY CLASSIF. (of this page) Unclassified		21. NO. OF PAGES 41	22. PRICE NTIS